The Pennsylvania State University

The Graduate School

DENSITY DISTRIBUTION EFFECTS ON THE SETTLING DYNAMICS OF NONSPHERICAL INERTIAL PARTICLES AT INTERMEDIATE REYNOLDS NUMBERS

A Thesis in

Mechanical Engineering

by

Brandon Angle

© 2019 Brandon Angle

Submitted in Partial Fulfillment
of the Requirements
for the Degree of

Master of Science

August 2019

The thesis of Brandon Angle was reviewed and approved* by the following:

Matthew Rau
Assistant Professor in Mechanical Engineering
Thesis Co-Advisor

Margaret Byron
Assistant Professor in Mechanical Engineering
Thesis Co-Advisor

Robert Kunz
Professor in Mechanical Engineering

Daniel Haworth
Professor in Mechanical Engineering
Head of the Department or Chair of the Graduate Program

*Signatures are on file in the Graduate School

ABSTRACT

In natural sedimentation, many particles of interest are both large and nonspherical. Some common particle types (e.g. naturally occurring aggregates) do not have a uniform mass distribution. As a result, the centers of mass and buoyancy are not co-located, leading to complex settling dynamics. Here we investigated the orientation and terminal velocity of initially horizontal, freely falling cylinders, in which the mass distribution was either constant (uniform-density, UD) or bipartite, undergoing a step change halfway along the length (compound-density, CD). Cylinders had relatively low aspect ratios ($1 \leq AR \leq 4$), and fell at intermediate Reynolds numbers (of order 100). We recorded the velocity, orientation, and landing site of each cylinder in quiescent flow. Results showed significant differences between the settling characteristics of uniform- and. compound-density cylinders. For cylinders with $AR = 1$, varying center of mass location (CD cylinders) led to a more predictable fall trajectory and orientation compared to UD cylinders. Varying the center of mass location for $AR = 2$ cylinders resulted in two different settling modes, demarcated by a transitional Reynolds number regime. For $AR = 4$ cylinders, varying the center of mass location did not produce as large an effect, but did lead to an angled settling trajectory with a pronounced off-horizontal orientation relative to the UD cylinders. All CD cylinders, regardless of aspect ratio, were biased to land on the side of the tank where the more-dense end of the cylinder was initially oriented. In general, cylinders with the smallest vertical projected area fell with the greatest terminal velocity; however, the mechanisms controlling orientation remain unclear. Our results have important implications for predicting the settling behavior of naturally-occurring particles, and lay the groundwork for further study of particles settling in complex flows such as turbulence. Given our results in still water, the net torque created by non-co-located center of mass and center of volume are likely to strongly impact particle motion in turbulence.

TABLE OF CONTENTS

LIST OF FIGURES

LIST OF TABLES

NOMENCLATURE

(x_c, y_c, z_c)	centroid location of a cylinder in global space
(x_{c1}, y_{c1})	centroid (*x*,*y*) of cylinder in High Speed Camera 1
(x_{c2}, y_{c2})	centroid (*x*,*y*) of cylinder in High Speed Camera 2
$(\mathrm{x}, \mathrm{y}, \mathrm{z})$	coordinate system for global space
A^*_{surf}	(dimensionless) normalized surface area: the ratio between the surface areas of the ellipsoidal particle and a sphere of equivalent volume
${C_D}^{*1}$	Schiller Neumann drag correction factor
${C_D}^{*2}$	Clift Gauvin drag correction factor
Re^*_p	adjusted Reynolds number calculated by applying Stokes and Newton regime drag correction factors
μ_f	dynamic viscosity of water
ρ_c	density of the cylinder
ρ_w	density of water
C_D	drag correction factor
C_{shape}	shape correction factor for the Newton regime
D_c	diameter of the cylinder
F_D	drag force
L_R	longest side length of the fitted rectangle bounding each cylinder within a single camera field of view
L_c	length of the cylinder
Re_p	particle Reynolds number based on volume-equivalent sphere diameter
SG_1	specific gravity of the less dense end of each compound density cylinder
SG_2	specific gravity of the uniform density cylinder
SG_3	specific gravity of the denser end of each compound density cylinder

d_{eq}	diameter of sphere with equivalent volume to a given cylinder
f_{shape}	shape correction factor for the Stokes regime
t_{95}	critical t-value for a t-test performed at the 95% confidence level
$\bar{u}$	average u between all trials in a cylinder class
$\bar{v}$	average v between all trials in a cylinder class
$\bar{w}$	average w between all trials in a cylinder class
x_{range}	range in x-direction each cylinder travels through the global space within both high speed cameras fields of view
z_{range}	range in z-direction each cylinder travels through the global space within both high speed cameras fields of view
γ_{xz}	angle between High Speed Camera 1 and High Speed Camera 2 in $x-z$ plane
θ_1	angle between positive x-axis and principal axis of cylinder in High Speed Camera 1
θ_2	angle between positive x-axis and principal axis of cylinder in High Speed Camera 2
σ_u	standard deviation of u between all cylinder trials within a class
σ_v	standard deviation of v between all cylinder trials within a class
σ_w	standard deviation of w between all cylinder trials within a class
σ_Φ	standard deviation of Φ between all cylinder trials within a class
σ_θ	standard deviation of θ between all cylinder trials within a class
ω_z	vorticity in the +z-direction
r	radial distance away from center of landing site target
u	velocity component in +x direction
v	velocity component in +y direction
w	velocity component in +z direction
Φ	angle between principal axis of cylinder and $x-y$ plane

θ	angle between principal axis of cylinder and $x-z$ plane

ACKNOWLEDGEMENTS

I would like to thank Dr. Matthew Rau and Dr. Margaret Byron for being extremely supportive over the last two years. Additionally, I want to thank my fellow lab mates for all the help and encouragement along the way.

I would also like to thank my parents, grandparents, and girlfriend for helping me gain the courage to believe in myself during this journey. This work is dedicated to everyone mentioned here.

Chapter 1: Introduction

1.1 Research Background and Motivation

Particles with a wide range of shapes and sizes play a key role in many natural and engineered processes, such as dispersion, sedimentation, the formation and transport of aerosols, waste-water treatment, and many more. Particles within these systems are often naturally irregular in shape or have aggregated through collision with other particles to form aggregates. Furthermore, the sedimentation of aggregates is responsible for the transportation of many nutrients. However, turbulent systems have complicated the settling dynamics of particles and aggregates making this transportation process poorly understood. A better understanding of the interaction between nonspherical particles and turbulence is necessary to better understand natural particle sedimentation.

Often large bodies of water (such as oceans, lakes, and rivers) exhibit turbulent flow conditions, which affect the behavior of plants, animals, or particles present in the flow. Turbulence is spatiotemporally variable and can differ significantly between different geographical locations and environments [1,2]. Three different regimes exist that describe how particles interact and are influenced by turbulence. The first regime is referred to as one-way coupling. Here, the particle volume fraction is small and particle inertia is low. In this regime, the particulate matter is influenced by the turbulent flow, but the particles do not modify the turbulence itself. If the volume fraction of particles is increased or if particles with more inertia (greater mass or velocity) are introduced to the flow, the particles become two-way coupled to the surrounding flow, where the particles influence the turbulence and the turbulence influences the particles. A single particle may be classified in the two-way coupling regime if the particle inertia is large. The third particle-

turbulence interaction regime is called four-way coupling. This regime exists when inertial particles have a significantly high volume fraction. Similar to two-way coupling, the turbulence affects particle motion while the particle causes turbulent enhancement or attenuation. However, four-way coupling also consists of particle-particle interaction, which occurs when a high volume fraction of particles leads to particle-particle collisions.

In turbulent environments that contain a wide range of particulates (*e.g*. natural bodies of water), aggregates are typically composed of many smaller individual particles, each with a unique density. These aggregates behave as a single particle, but can have very irregular shapes and non-uniform density distributions [3]. Despite the prevalence of irregular particles and particle aggregates, much of our current knowledge of suspended particle sedimentation behavior is based on theory derived for spherical or ellipsoidal particles of uniform density [4,5], which are not always representative of real particulate matter of interest. Thus, it is important to develop an understanding of the distinct settling behavior of non-spherical particles with non-uniform density to improve our understanding and predictive capabilities of the fate of particulate matter in natural systems.

Particle settling behavior is typically described based on the particle Reynolds number (Re_p). Previous work has primarily focused on settling particles in Stokes flow ($Re_p < 1$) for spherical [1,6] and nonspherical [7–10] particles as well as at high Reynolds numbers ($Re_p >> 1$) for spherical [11,12] and nonspherical [13–15] particles. However, nonspherical particle behavior at intermediate Reynolds numbers (Re_p of order 10-100) remains comparatively understudied. Additional investigation of particle settling behavior at these Reynolds numbers is warranted given how many particles of interest to the natural and built environment fall into this regime (*e.g*. large sediment particles, marine aggregates, and even semi-passive planktonic larvae [16].

Here, we present an experimental study of non-spherical inertial particles with non-uniform density, settling at intermediate Reynolds numbers. Following a brief discussion of the current state of the field we introduce a fabrication method, which allows for cylindrical particles to be cast out of layers of hydrogel of different density to create nonspherical particles without co-located centers of mass and volume. We use high-speed imaging to measure the velocity, orientation, and other variables of interest as the cylinders fall and present our results in the context of applications in engineering.

1.2 Literature Review

1.2.1 Particle Characteristics

Solid-liquid flows can have a very wide range of diverse particle types, including everything from perfectly round micron-sized glass spheres [17] to large pieces of debris floating in rivers and canals [18]. While manufactured particles often have a regular shape (*e.g.* spheres), this is not the case for naturally occurring particles, which may be nonspherical. Naturally occurring particles can include delicate [19–22] or degradation-resistant [23,24] particles over various sizes [25–27].

An example of large irregular particles are rocks and boulders that exist in debris flows. Here, the large boulders or other debris has the ability to shape rivers, canals, mountains, and more [23,28]. Events such as mudslides, volcano eruptions, and flash floods often initiate debris flows consisting of largely nonspherical particles. Unfortunately, this also means debris flows also have the ability to harm communities. Therefore, it is import for scientists and researchers to be able to predict when and where debris flows will develop. Recently it has been discovered that large particles in debris flows often end up settling to the bottom of ocean floors. This sedimentation process transports marine sediments and nutrients to deeper depths of the ocean [29]. However, this transportation process occurs less frequently than the transportation and sedimentation process of marine nutrients through marine aggregates.

Marine aggregates are difficult to characterize because they exist across a wide range of sizes and are made of a variety of materials. These materials can include phytoplankton, sand, dirt, animal waste, and other debris, sometimes held together by bacterial exudates. As the marine aggregates fall from the surface of the ocean to the ocean floor, each aggregate continually gains and loses matter through aggregation, disruption, and remineralization. The structure and strength

of aggregates has been observed to change throughout the collision process [32]. Two mechanisms governing particle aggregation are Brownian motion and shear aggregation. Brownian motion is relevant to submicron-sized particles [33,34], whereas shear aggregation, which describes the collision of particles in laminar and turbulent flows, is relevant above the submicron range [35]. Turbulence can increase or decrease aggregation rates depending on the shear rate within the flow [35,36]. A collision between two aggregates in turbulence results in either breakup or further aggregation. Both outcomes change the structure, shape, and the distribution of material (*i.e*. the density distribution) of the aggregate. However, the transportation of carbon and other nutrients throughout large bodies of water is still mostly undetermined due to the complexity of aggregate structures and settling behaviors.

The wide variations in aggregate size, shape, and mass can lead to complex variations in their settling velocity [20]. Over a long period of time, aggregates will become composed of a large number of materials and components each with a unique density. Therefore, the center of mass of each aggregate depends on the location of the denser materials. Additionally, it is likely the aggregate center of mass (COM) will be located at a distance away from the aggregate center of buoyancy (COB) resulting in unique particle settling behaviors. Measured aggregate diameters are typically on the order of tens of micrometers to centimeters [30], with extreme cases up to a few meters in size [22]. The size and shapes of naturally-occurring aggregates have been documented to vary seasonally [31], additionally contributing to the complexity of predicting particle behavioral characteristics.

1.2.2 The influence of particle shape on settling behavior

A particle Reynolds number can be defined for an irregular shape based on the diameter of a sphere with equivalent volume.

$$Re_p = \frac{\rho_f v d_{eq}}{\mu_f}, \tag{1}$$

where ρ_f is the density of the fluid, v is the terminal settling velocity, d_{eq} is the diameter of the sphere of equivalent volume, and μ_f is the dynamic viscosity of the fluid. This particle Reynolds number is the most important parameter in determining the settling velocity of a spherical or nonspherical particle, and is thus the basis for many drag coefficient calculations.

In the Stokes regime ($Re \ll 1$) , the drag force acting on the particle is proportional to the first power of terminal settling velocity shown in Equation (2)

$$F_D = -3\pi d_{eq} \mu_f v, \tag{2}$$

and in the Newton regime ($Re \gg 1$) drag force is proportional to the terminal velocity squared as shown in Equation (3)

$$F_D = -\frac{\pi}{8} {d_{eq}}^2 \rho_f C_D v^2, \tag{3}$$

where C_D is the drag correction factor. However at intermediate regimes, the drag force is proportional to some power of velocity between one and two and therefore needs correction factors to maintain validity. Analytically determining terminal settling velocity and Reynolds number for particles with simple shapes is straightforward in the Stokes regime [4]. Empirical relationships also exist for calculating the same quantities in the Newton regime ($Re_p >> 1$). However, calculating these quantities is much more complicated at intermediate Reynolds numbers, where complex wake dynamics prevail [37]. For simplicity, early studies of particles settling in this Reynolds number regime primarily characterized spherical particles [38–41].

Early models to predict nonspherical particle behavior primarily involved corrections to models for spherical particles. Leith [10] related nonspherical particle projected area and surface area to that of a sphere. From previous studies and correlations, a dynamic shape factor, K, could be calculated and added to Equation (2) as an additional term on the right-hand side. This method was attractive due to its simplicity, but was also susceptible to rather large errors since it fails to capture the variability of more complex particle shapes. Chhabra *et al*. [42] later expanded on these models for irregularly shaped particles by introducing particle sphericity. Here, the surface area of a sphere with equivalent volume to the particle was normalized with the surface area of the particle. Sphericity within this study ranged from 0.1 for discs to 1 for spheres and is applied to drag coefficient equations to better estimate a particle Reynolds number ranging from 10^{-4} to 10^{5}. Furthermore, Tran-Cong *et al*. [43] introduced two correction factors to calculate the settling velocities of irregular shaped particles at Reynolds numbers from $0.15 < Re_p < 1500$. The first correction factor they introduced was the particle circularity, which was defined as the projected area of a sphere, with surface area equivalent to that of the irregular particle, normalized by the projected area of the particle in the direction of motion. The second correction factor, called the flatness ratio, was defined as the diameter of a sphere with equivalent surface area normalized by the volume-equivalent sphere diameter. Each of these correction factors can be added as a correction factor to the drag coefficient calculation and is accurate for extremely irregular shapes.

Loth [4] represented nonspherical particles as ellipsoids with varying aspect ratios (AR) in the Stokes regime and Newton regime. He accounted for shape variations through the projection of the particle shape in the direction of motion. Here, the maximum projected area was used to predict the fall orientation. This model was derived for low aspect ratio ellipsoids ($AR \sim 1$) at intermediate Reynolds numbers. In short, this model determines correction factors for the Stokes regime equations using the ellipsoid shape and aspect ratio to extend the range of validity to intermediate Reynolds numbers.

With Re_p and v unknown in Equation (1) for nonspherical shapes, additional information is necessary to determine terminal settling velocity. A force balance is necessary between the drag force, gravitational force, and counteracting buoyancy force. Equating the drag force to the difference of the other two forces allows the terminal vertical velocity of the particle to be calculated through an additional equation. However, two shape variation parameters must be calculated to accurately determine the vertical velocity for these nonspherical particles. An adjusted Reynolds number can then be iteratively calculated by applying a Stokes and Newton regime drag correction factor to the previously defined particle Reynolds number

$$Re_p^* = \frac{C_{shape} Re_p}{f_{shape}}, \tag{4}$$

where C_{shape} is the drag correction factor for shape variation in the Newton regime and f_{shape} is the drag correction factor for shape variation in Stokes regime. Equation (4) is only valid at intermediate Reynolds numbers as it incorporates corrections from the two extreme regimes Additional equations, outlined in full in [4] and summarized here, are used to calculate both of these correction factors. For ellipsoids, Equation (5) relates the Stokes regime drag correction factor to the aspect ratio

$$f_{shape} = \frac{AR^{1/3}\sqrt{AR^2-1}}{\ln(AR+\sqrt{AR^2-1})}. \tag{5}$$

Equation (6) relates the Newton regime shape correction factor to the surface area of the ellipsoid:

$$C_{shape} = 1 + 0.7\sqrt{A_{surf}^* - 1} + 2.4\left(A_{surf}^* - 1\right), \tag{6}$$

where A_{surf}^* is the (dimensionless) normalized surface area: the ratio between the surface areas of the ellipsoidal particle and a sphere of equivalent volume. Equation (7) shows the same relationship for a cylinder:

$$A_{surf}^* = \frac{2AR+1}{18AR^{2\frac{1}{3}}}. \tag{7}$$

With a corrected Reynolds number, we can now apply the Schiller-Neumann and Clift-Gauvin drag correction factors to get an overall corrected drag coefficient, suitable for predicting a nonspherical particle's settling velocity. The Schiller-Neumann correction coefficient is given by Equation (8) as

$$f_{RE} = 1 + 0.15(Re_p^{*0.687}). \tag{8}$$

Equation (8) helps correct the drag coefficient for nonspherical particles and is accurate up to $Re_p < 800$. The overall corrected Newton-regime drag coefficient from Schiller-Neumann can then be calculated as

$$C_D{}^{*1} = f_{RE}(\frac{24}{Re_p^*}). \tag{9}$$

A second correction factor, the Clift-Gauvin factor, is also necessary and is calculated following

$$C_D{}^{*2} = \frac{0.42}{1+\frac{42{,}500}{Re_p^{*1.16}}}. \tag{10}$$

The Clift-Gauvin correction factor further corrects Stokes equations up to $Re_p < 2 \times 10^5$. The final overall correction factor for the Stokes equations is the sum of the two drag correction factors in Equations (9) and (10)

$$C_D{}^* = C_D{}^{*1} + C_D{}^{*2}. \tag{11}$$

From this overall correction factor, we can calculate a corrected drag coefficient for the Newton regime using

$$C_D = C_D{}^* C_{shape}\,. \tag{12}$$

The overall drag force for intermediate Reynolds numbers can then be defined through Equation (3).

1.2.3 Settling Cylinders of Uniform Density

While ellipsoidal particles are frequently featured in numerical studies of nonspherical particles [13], cylinders are commonly used for experimental studies due to greater ease of manufacturing [44–47]. The settling trajectories of cylinders with aspect ratios less than one (*i.e.*, disks) have been experimentally studied by Kanso *et al.* [45]. They showed that there are four distinct settling motions for these particles: steady, fluttering, chaotic, and tumbling. These settling modes yield unique landing site probability density functions for each disk AR, which can be used to reliably predict what side of the disk is most likely to land upright. Mandø and Rosendahl [14] determined that freely falling cylinders with any aspect ratio and uniform density must fall with either a steady orientation or periodic motion. Cylinders with $AR < 2$ had little resistance to tumbling motion, making it difficult to predict settling behaviors. Tumbling is defined as when the major axis of the cylinder rotates end-over-end during settling. Higher aspect ratio cylinders showed greater resistance to tumbling and fell with a steady orientation.

Komar [8] compared the settling velocities of uniform-density cylinders ($2.05 < AR < 11.45$) to settling velocities of uniform-density ellipsoids of equivalent aspect ratio. Results showed an increased drag coefficient for cylinders due to their increased surface area when compared to an equivalent AR ellipsoid. Marchildon *et al.* [48] studied the wakes of freely falling circular cylinders ($1.46 < AR < 35$) at Reynolds numbers between 70 and 2400. Periodic oscillations were never present in the cylinder wakes when $Re < 80$ and always present when $Re > 300$, where Reynolds number was calculated with the particle lengthscale based on maximum projected area. Mandø and Rosendahl [14] found that freely falling cylinders with $Re_p > 100$ of both low and high AR have significant oscillatory motion due to particle wake instabilities. These data for cylinders indicating the onset of wake instabilities for Reynolds numbers between 100 and 300 correspond well to a previous study of freely falling spheres at intermediate Reynolds

numbers, which showed that the vortex ring behind falling spheres detaches around $Re_p = 210$, creating an oscillating vortex structure in its wake [37,49]. In comparison, the transitional Reynolds number for an infinitely long cylinder is around 100.The wake transition Reynolds number for cylinders is lower than it is for spheres because a sphere has an extra degree of freedom for fluid to move around it.

Chung *et al.* [50] provided one of the only studies to experimentally investigate the behavior of cylindrical particles at intermediate Reynolds numbers with aspect ratios close to one. They studied the wake characteristics of tethered, low aspect ratio cylinders ($0.5 < AR < 2$), where a wire strung through the center of the cylinder allowed for one degree of freedom in a horizontal water channel. While this is not exactly analogous to settling (gravity is acting perpendicular to the direction of flow in this case), their results are relevant to settling cylinders at similar Reynolds numbers and aspect ratios. Their results showed three modes for the hinged cylinders as the Reynolds number varied from 100 to 5000, where Reynolds number was defined by the length of the cylinder perpendicular to the flow. Intermediate Reynolds numbers showed steady and periodic orientations, while cylinders at high Reynolds numbers displayed auto-rotation around the hinged axis.

1.2.4 Settling Cylinders with Varied Centers of Mass

Particles with compound densities have seen fewer investigations than those with uniform density. A compound density cylinder refers to a cylinder where the COM is in a different location than the center of volume. Yasseri *et al.* [51] focused on the importance of predicting the landing site for cylinders that were 9 to 15 cm long, with aspect ratios between one and two, settling in water with velocities between 1-10 m/s. These settling velocities are common for pipes, tanks, and other equipment commonly delivered to construction projects beneath the water surface. They

tested cylinder drop angles from 15° to 75°, defined as the angle between the principle axis of the cylinder and the horizontal. Their cylinders were fabricated with an internal weight, whose position was varied using a threaded rod to alter the location of COM of the cylinder. It was determined the COM position influenced the cylinder trajectories significantly and had a greater influence on landing site than the initial inclination drop angle or cylinder aspect ratio. Their results showed that 98% of cylinders with low aspect ratios ($1 < AR < 2$) and off-center COM land within a radius that is less than 50% of the water depth.

The behavior of cylinders with large aspect ratios and nonuniform densities are also useful for Naval research applications. Abelev *et al.* [52] discovered that cylinders at high Reynolds numbers fell with a greater terminal velocity when the center of mass was furthest from the geometric center of the cylinder. Similar results were obtained by Lan *et al*. [53], who showed six different cylinder trajectories (straight, spiral, flip, flat, seesaw, combination), which were dependent upon center of mass location. When the center of mass was co-located with the center of buoyancy, the cylinder fell with a flat orientation with the major axis of the cylinder perpendicular to the settling direction. As the mass was varied along the length of a cylinder, the cylinder began to rotate and fall with oscillatory motion. Results once again showed that the COM location significantly affected the cylinder trajectory, while initial cylinder orientation and velocity had little impact on trajectories.

While these (few) studies have varied the center of mass location in falling cylinders, the Reynolds numbers were high compared to the intermediate Reynolds numbers of relevance to natural particles and aggregates in the environment. Studying cylinders over a wider range of aspect ratios, Reynolds numbers, and mass distributions will help determine when certain settling regimes are relevant to predicting the fall behavior of these particle types.

1.2.5 Cylinder Fabrication Methods

Previous studies fabricated cylindrical particles using numerous different methods, including machining raw material to match specific dimensions [13], cutting glass cylinders out of a solid rod with desired diameters [9], and punching cylinders out of a solidified solution [54]. Recently, 3D printing has allowed researchers to print particles with nonstandard shapes like 2D and 3D crosses where the 3D crosses were referred to as jacks [55]. However, multiple limitations exist with 3D printing such as cost, porosity, and printer resolution. A general limitation to particle fabrication is the need to produce large numbers of particles in a short timeframe. Additionally, designing cylinders to fall within a specific Reynolds number regime can be difficult due to limited material densities. Increasing or decreasing the density of material for a certain volume cylinder will increase or decrease the cylinder mass respectively. A cylinder with greater mass will reach a greater terminal velocity if volume is kept constant. Often, particles with large dimensions are desired for visualization accuracy. Therefore, large cylinders falling at intermediate Reynolds numbers must have a material density close to that of the fluid surrounding them.

Hydrogel particles have the ability to be molded into various shapes for different applications. In biomedical applications, hydrogel particles are readily fabricated for 3D cell studies, with injection molding typically being used to form hydrogel material into defined sizes and shapes at the nano scale [56]. Other studies have shown hydrogels maintain stable properties in varied pH, temperature, and tonicity[57,58]; this stability has enabled other studies to expand the application of hydrogels. Byron and Variano [59] fabricated hydrogel ellipsoids to study flow structures around the ellipsoids using tracer particles. Hydrogel cylinders have also recently been used to understand the rotational kinematics of large cylindrical particles in turbulence [60].

In this thesis, we fabricate cylindrical particles using hydrogel. Advantages of hydrogels include their ability to be poured as a liquid and cool as a solid, which allows us to successively

pour solutions of different density into molds to fabricate cylinders. The density of hydrogels is also precisely controllable and very close to that of room temperature (20℃) water. This relatively low specific gravity allows us to fabricate particles at intermediate Reynolds number with a lower absolute settling velocity but a large size, which is beneficial to our visualization-based measurements. Hydrogels also have a similar refractive index as water, which aids particle image velocimetry (PIV) measurements as the hydrogel does not block or reflect laser light used for the measurements [59,60].

In this thesis, we provide the necessary foundation for examining the settling behavior of compound density particles falling at intermediate Reynolds number in quiescent flow, specifically studying particle terminal velocity, orientation, and trajectory. This study narrows the gap in our knowledge of the settling behavior of nonspherical particles with compound densities. A better understanding of these behaviors exhibited by cylinders in free fall at intermediate Reynolds numbers will inform studies of natural sedimentation and dispersion processes, as well as the design of engineering applications involving solid-liquid multiphase flows. This study also serves as a first-step towards studying nonspherical particles with compound densities in turbulence.

Chapter 2: Methods

2.1 Hydrogel Density Validation

The density of agarose hydrogel can be precisely controlled by increasing or decreasing the concentration of powder used in the liquid solution prior to solidification. We needed to determine the density of different concentrations of hydrogel solutions as a first step in designing our cylinders to fall at intermediate Reynolds numbers. The density of hydrogel was measured as a function of agarose powder concentration by recording the terminal settling velocity of spheres with known-diameters manufactured with different hydrogel concentrations. Determining terminal velocity for spheres is straightforward because their drag coefficients are fully mapped from low to high Reynolds numbers [4]. For our density validation experiment, a high speed camera (AX200, Photron) was used to capture the position of the centroid of a hydrogel sphere as a function of time as it fell in 20℃ still water. The field of view of the high speed camera was centered 37.5 cm below the dropping mechanism to ensure the spheres had reached terminal velocity before their velocity was recorded (verified by plotting the vertical velocity over time for each sphere and confirming that it remained constant).

Hydrogel spheres were made by injecting heated solutions of agarose powder (OmniPur Agarose, Calbiochem) and water with a syringe into three identical 3D-printed spherical molds with a sphere diameter of 1 cm. The solution cooled at 20℃ for 10 minutes before being additionally cooled in a refrigerator for 3 minutes. The three spheres were removed from the molds and dropped one at a time in the tank described in Section 2.4 Experimental Setupwhere their terminal velocity was measured. Each of the three spheres was tested three times, and the manufacturing process was repeated to generate more spheres to increase the robustness of the measurement. Surface defects caused by handling were typically visible on each sphere after three

drop attempts; measurements were discontinued if defects were significant and likely to lead to a change in fall velocity. A total of 15 to 20 trials were recorded for each agarose concentration; five different concentrations of agarose powder were tested to determine the influence of agarose concentration on hydrogel density. Density calculation for each sphere was accomplished by first setting the net gravitational force equal to the drag force (which is a function of velocity and drag coefficient). Since the drag coefficient is a function of velocity, the density was iterated until both forces were equal. Figure 1 shows the average calculated density for the five different concentrations tested in this experiment. There is an increasing linear trend in density for all five recorded concentrations. Agarose powder has a density greater than that of water, so an increase in density for higher Agarose concentrations was expected. 0.008 g/mL was the smallest concentration that resulted in cohesive spheres; lower concentrations produced spheres which could not be handled without falling apart. The additional four concentrations were chosen so the hydrogel densities would remain close to that of room temperature water (20℃), which facilitated the fabrication of nearly neutrally buoyant cylinders as described in the next section. Because we were interested in creating cylinders which are close to neutral buoyancy, the upper bound of the tested density range was chose to have a specific gravity no greater than 1.01. This facilitated the fabrication of the four additional concentrations.

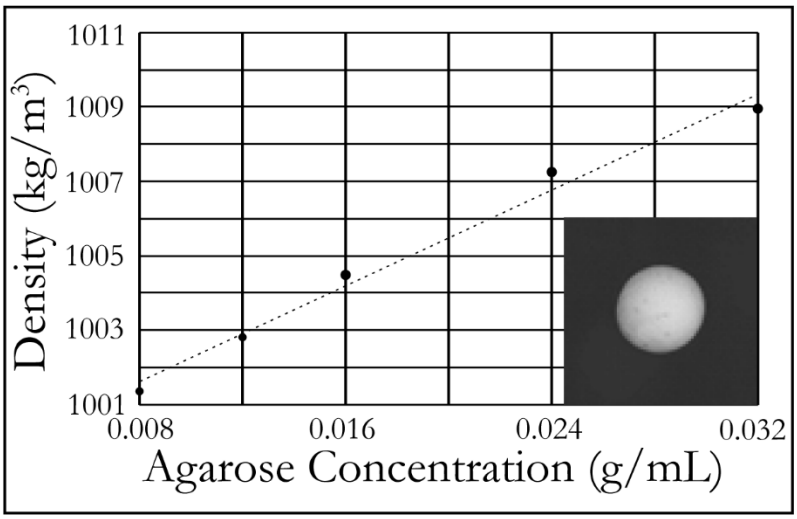

Figure 1. Hydrogel density for different Agarose concentrations, iteratively calculated via terminal velocity measurements of spheres using the model of Loth for intermediate Reynolds number particles [4] *. The insert figure is an image of a hydrogel sphere used during testing.*

2.2 Cylinder Design Process

As mentioned previously, the cylinder shape was selected because it is easy to fabricate and provides a good starting point for the general study of nonspherical particles. Three relatively low aspect ratios were chosen for our cylinders: 1, 2, and 4. Three Agarose concentrations at the lower end of the density range shown in Figure 1 (0.008, 0.012 and 0.016 g/mL) were selected, which allowed the cylinder dimensions to be maximized while targeting a specific Reynolds number. Two classes of cylinders were fabricated for each aspect ratio, as shown in Figure 2. Cylinders with uniform density (UD) were fabricated using the intermediate hydrogel density (specific gravity of 1.005). Cylinders with compound density (CD) were fabricated in a two-step process, with one half being made out of hydrogel with a specific gravity of 1.003 and the other with a specific gravity of 1.007. These concentrations were chosen so that both the UD cylinders and CD cylinders for a given aspect ratio had the same overall mass (and therefore the same average density). The particle Reynolds number given in

Figure 2 is calculated using the volume-equivalent sphere diameter. We chose to use volume-equivalent sphere diameter since our cylinder aspect ratios are close to one, more closely resembling spheres than infinitely long cylinders. To design the dimensions of each cylinder to be used for testing, the vertical velocity of each prospective shape was first predicted using the Loth model [2]. The major and minor axis lengths were then tailored to match desired particle Reynolds numbers for the chosen cylinder aspect ratios.

A Reynolds number of $Re_p = 210$ was targeted for each cylinder, previously recorded as a transitional Reynolds number for the wakes of spheres and cylinders [14,49]. Cylinders descending with very low Reynolds numbers have attached vortex structures. As the particle Reynolds number increases, the attached vortex structures behind the cylinder become detached and shed periodically. This threshold of the breaking of axisymmetry in the wake occurs around $Re_p = 210$; it is this transition we have chosen to target in our experiments.

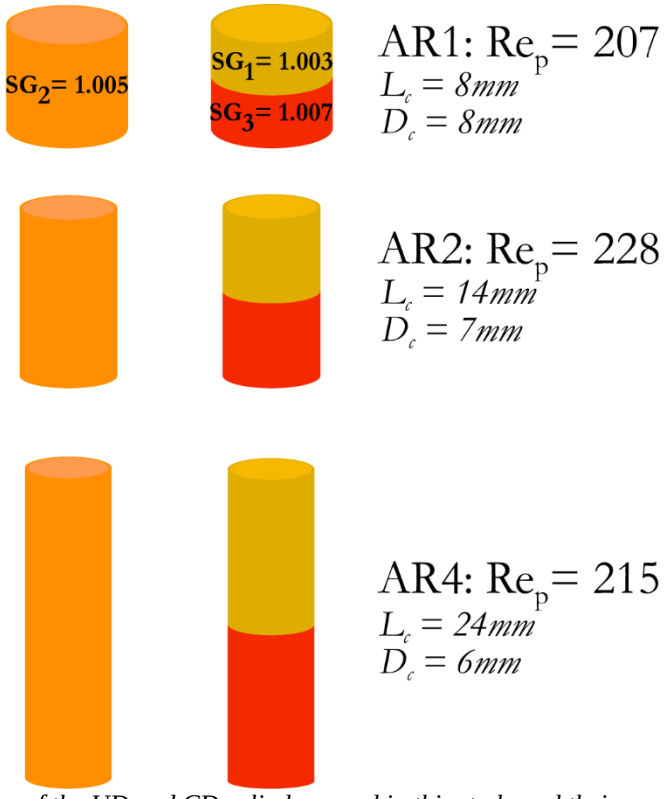

Figure 2. Drawings of the UD and CD cylinders used in this study and their predicted particle Reynolds number Re_p, which was calculated using the volume-equivalent sphere diameter and the velocity predicted from intermediate-Re settling models outlined in [4].

2.3 Cylinder Fabrication

The first step of cylinder fabrication was mixing the appropriate amount of agarose powder with 50 mL of distilled water to achieve the desired concentration. Next, the solution was constantly stirred and heated to a temperature of 175˚F. This temperature was maintained for 25 minutes, allowing the agarose power to fully dissolve. A hot water bath provided uniform heating to the entire solution volume. A prescribed volume of the heated solution was then injected into machined aluminum molds using an adjustable micropipette (set to the desired volume). UD cylinders were

made by filling the entire mold with one (constant-density) hydrogel solution. CD cylinders were fabricated by first half-filling the molds with one solution (lower density), followed by the second (higher density) after a three minute interval. The solution with the highest specific gravity ($SG = 1.007$) was too dense to distribute with a micropipette. Therefore, for all CD classes, the molds were first half-filled with the solution with $SG = 1.003$ using a micropipette and then completely filled with $SG = 1.007$ solution using a standard transfer pipette. The two hydrogel solutions reliably bonded using this fabrication procedure. One CD cylinder batch (approximately 30 cylinders) for each aspect ratio was tested in free fall to verify that no separation occurred between layers. Figure 3 shows photographs of (A) the solution during heating, (B) a solidified CD cylinder, and (C) an aluminum mold used during fabrication. After both solutions were injected into the mold, the cylinders cooled at $20℃$ for 10 minutes before being placed in a refrigerator for an additional three minutes.

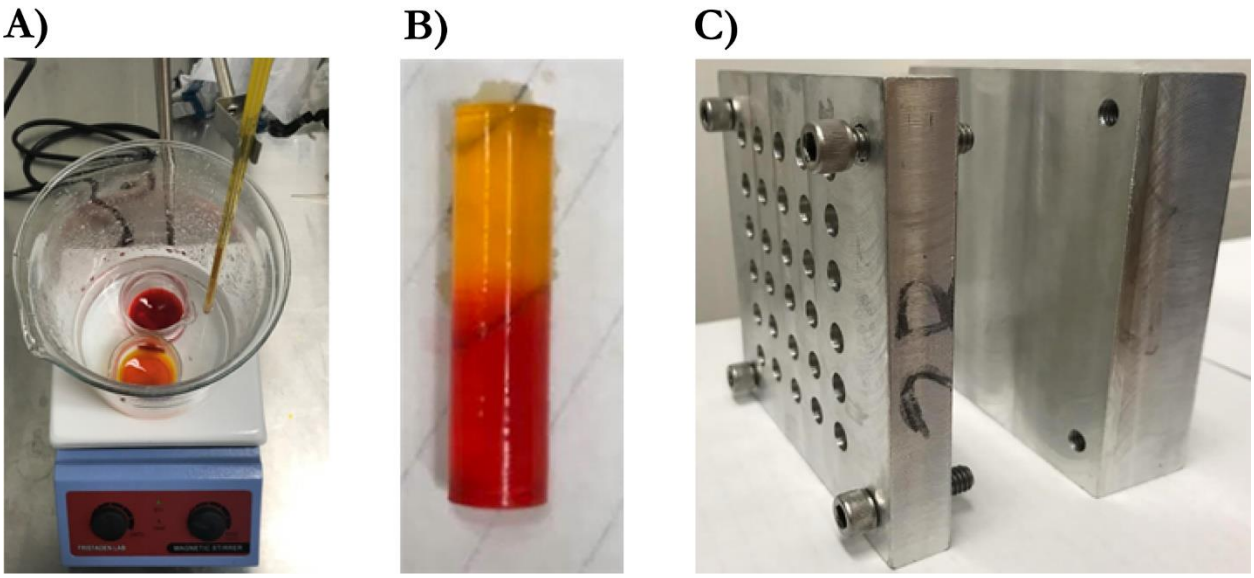

Figure 3. Photos of the cylinder fabrication process, including (A) the hot water bath used to heat the hydrogel solutions and dissolve the agarose powder, (B) a completed $AR = 4$ CD cylinder, and (C) one of the machined aluminum molds. In (A) and (B), the hydrogel solutions are dyed red ($SG = 1.007$) and yellow ($SG = 1.003$) to provide a visual cue for density differences. The volume of dye added was negligible and did not affect the density.

2.4 Experimental Setup

A diagram of the experimental facility is shown in Figure 4. The experimental facility consisted of a hexagonal water tank (61 cm in height with a parallel side-to-side width of 53 cm) filled with still water and a pair of modified forceps fixed 56 cm above the bottom of the tank and positioned just below the water surface. Two high speed cameras (AX200, Photron) captured cylinder orientation and terminal velocity through overlapping 15 × 15 cm fields of view centered 37.5 cm below the dropping mechanism. The viewing axes of the cameras were positioned perpendicular to the tank walls, separated by 120° in order to capture three-dimensional cylinder motion. Each cylinder was released in an initially-horizontal orientation, with the axis of symmetry perpendicular to the optical axis of High Speed Camera 1. For the compound-density classes, the denser side was initially on the left side of the field of view of High Speed Camera 1. The width of the tank was approximately 20 times the largest cylinder dimension of 2.4 cm (the length of the $AR = 4$ cylinders). Two LED light panels provided illumination for the high speed cameras. Images were acquired at 500 fps.

A low speed camera (RX100M4, Sony) was positioned directly on top of High Speed Camera 1 to capture an enlarged view of the tank, approximately 50 cm in height and 30 cm in width. Use of this camera allowed for qualitative visualization of the entire cylinder trajectory from the top to the bottom of the tank (but was not used for quantitative analysis). A second low speed camera (RX100M4, Sony), imaged the bottom of the tank *via* a mirror angled at 45º; this camera recorded the landing site for each cylinder (relative to the tank center, vertically aligned with the release location), as shown in Figure 4. To facilitate the recording of landing site location, a transparent target with concentric demarcations, centered with the cylinder dropper, was added to the bottom of the tank. This camera was triggered manually to capture still images at the moment when the cylinder impacted the bottom tank surface. The entire facility rested on an optical table.

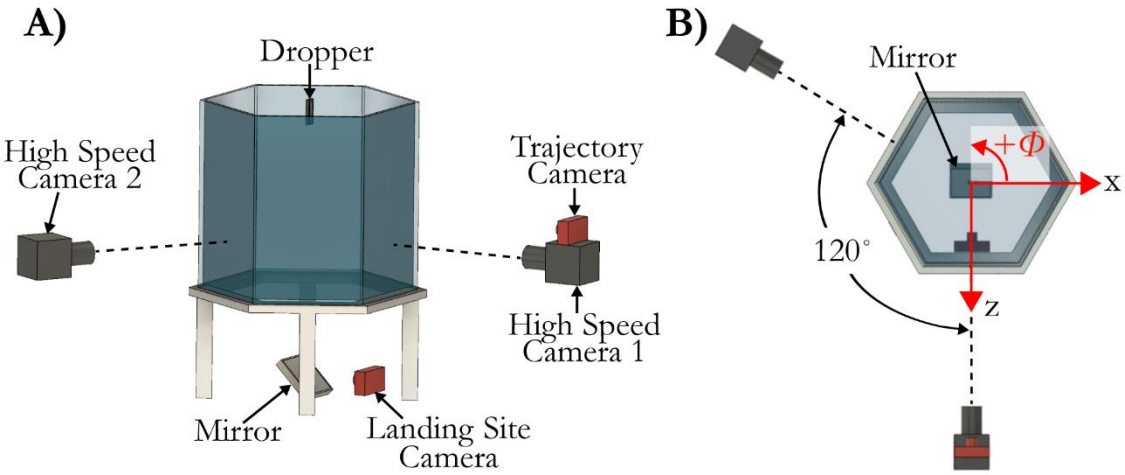

Figure 4. Experimental setup shown from (A) an isometric view, and (B) the top view, showing high speed cameras, low speed cameras, dropping mechanism, and mirror used to visualize landing sites. The angular coordinate Φ and global position coordinates (x and z) are also shown .

The flow fields around each cylinder class were also quantified in separate experiments using Particle Image Velocimetry (PIV). For these experiments, the flow was seeded with 55 μm polyamide spheres, which served as flow tracers. High Speed Camera 1 was used to capture planar PIV measurements of the cylinders and the surrounding liquid motion at an effective framerate of 50 fps ($\Delta t = 0.02$ s). The flow field was illuminated using a planar laser light sheet introduced through the bottom of the tank, as shown in Figure 5. A continuous-wave green laser (Opus 532, Laser Quantum) was positioned on the optical table in place of the landing site camera; the landing site target on the bottom of the tank was removed so as to not obstruct the laser light. A spherical convex lens (with a focal length of 0.5 m) narrowed the laser beam from 1.3 mm to an approximate minimum thickness of 0.2 mm in the field of view. The beam was reflected upwards by an optical mirror angled at 45°, and expanded into a sheet through a laser line generating optic (75° fan angle Laser Line Generator, Edmund Optics). The laser sheet was oriented perpendicular to High Speed Camera 1.

All PIV analysis was performed in the open source program PIVlab, a free MATLAB toolbox [61]. Images were pre-processed within PIVlab using an enhanced local contrast filter with

a 20 × 20 pixel window size, followed by a high-pass filter with a 15 × 15 pixel kernel. During processing, a multi pass scheme calculated vector fields with interrogation areas of 64 × 64, 32 × 32, and 24 × 24 pixels, each with a 50% overlap. This provided a final measurement resolution of 1.9 × 1.9 mm.

Post-processing included the removal of any velocity vectors greater than 15 standard deviations above the average velocity vector in each image. Vorticity in the flow was calculated by first smoothing the velocity vectors with a penalized least squares method [62] and then calculated as described by [63], shown in Equation (13):

$$\omega = \frac{dv}{dx} - \frac{du}{dy}. \tag{13}$$

These vorticity calculations were used to qualitatively evaluate wake structures around the cylinder.

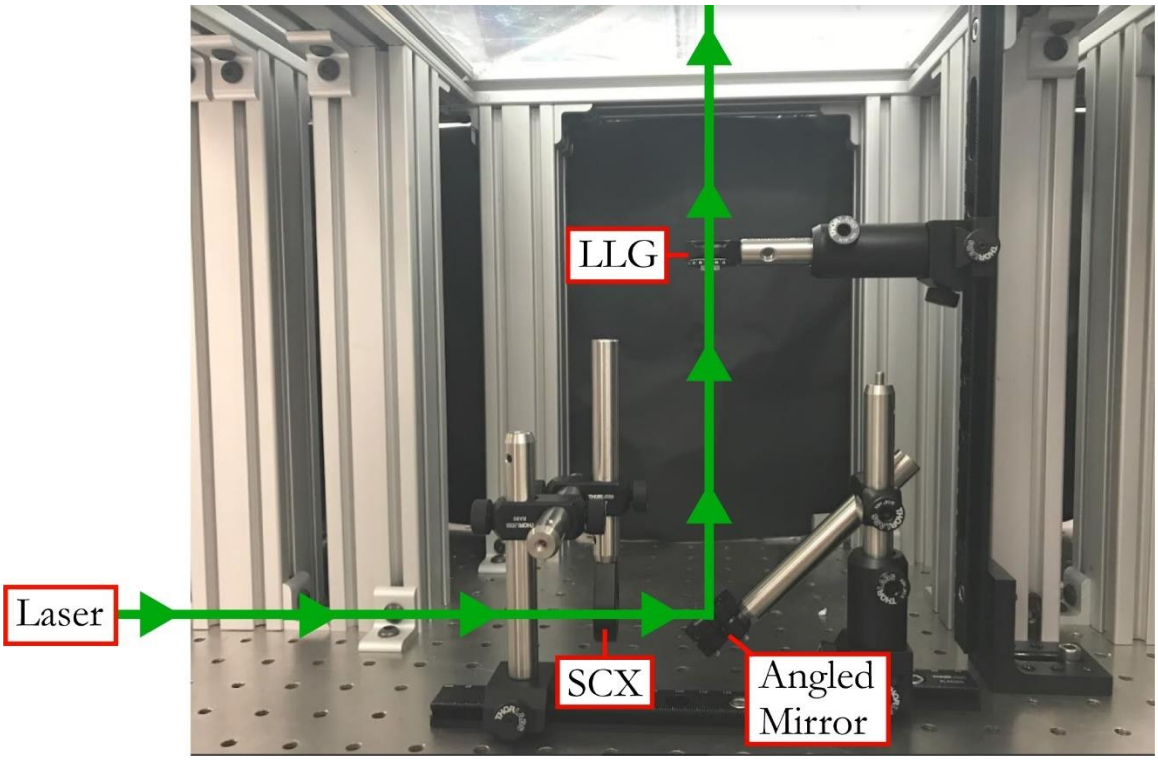

Figure 5. Laser sheet generation optical setup for PIV experiments. The beam first passes through a spherical convex (SCX) lens, which converges the beam to a narrow waist centered in the field of view of High Speed Camera 1. It then is reflected from a mirror at 45°, and passes through a laser line generator (LLG) before fanning out into a thin sheet.

2.5 Cylinder Centroid, Orientation, and Velocity Determination

To analyze the settling characteristics of each cylinder, its position in three-dimensional space needed to be identified as a function of time. These 3D positions were calculated from the combined two-dimensional image information from each high speed camera using MATLAB (Mathworks Inc.). To compensate for shifts in lighting during the experiment period, an average background image was subtracted from the first half of the experimental trials. Improvements in lighting quality for subsequent experiments allowed us to subtract only a minimum background image from the remaining experimental images. These image pre-processing steps improved image

quality and the reliability of subsequent analysis; a more detailed discussion of lighting can be found in Appendix A. After the background subtraction, the image was binarized using an adaptive threshold of .01 (the lowest possible threshold) for each image. This binarization often yielded multiple white regions, many of which were not correlated to the cylinder position. Therefore, additional processing was necessary to remove these noisy regions from the images, which frequently occurred around the image border. The noise regions were distinguished from the cylinder itself and eliminated from the image through their shape, their size, or their proximity to the border of the image. These processing steps resulted in a binary image, with the cylinder appearing as a lone bright white object on a black field. An additional processing step filled in any black spots contained within the cylinder boundary, which occasionally occurred if the image brightness was not consistent over the entirety of the cylinder. To further increase confidence in tracking the cylinder, the first image in each time series was displayed on screen and the initial cylinder location was manually confirmed. A timeseries of the 2D cylinder centroid location (x_{c1},y_{c1}) and (x_{c2},y_{c2}), in each camera's image plane (as labeled in Figure 7), was then calculated from the binary images of the cylinder projected area. As a final check on data quality, the time-history of the cylinder centroid location was used to prevent the centroid tracking from detecting and "jumping" to occasional image noise (which sometimes persisted through the image binarization despite exhaustive preprocessing), so that these regions were not erroneously labeled as the falling cylinder.

Once each image had been binarized and the cylinder centroid had been determined, the orientation of each cylinder in each camera's image plane was determined by fitting a rectangle to each binary cylinder projection. This process determined the pixel locations of the four corners of the cylinder in each camera image, as shown in Figure 6. From these corner locations it was then possible to determine the projected cylinder's minor and major axis length in each camera image plane. For $AR = 1$ cylinders, the major and minor axes were identical in length, rendering

automated determination of major vs. minor axes difficult. Therefore, the unprocessed high speed videos were manually checked to determine which rectangle side correlated with the axis of

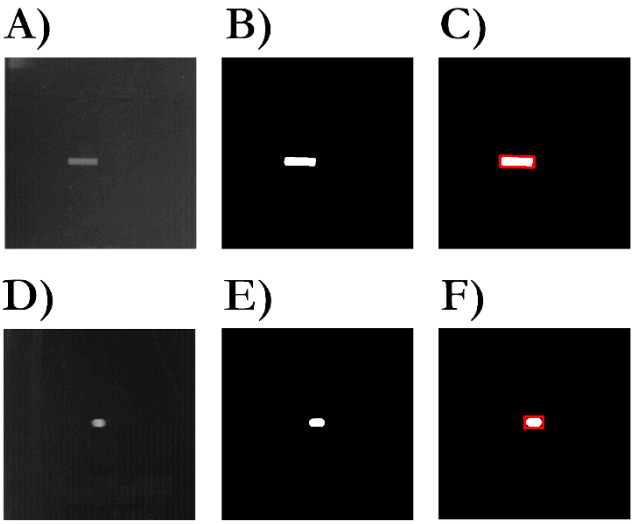

Figure 6. Process to determine four bounding points around each cylinder in High Speed Camera 1 (A-C) and High Speed Camera 2 (D-F) moving from original image, to binary image, to a fitted rectangle.

symmetry. Once the axis of symmetry of the cylinder was known for the first image, its orientation angle with respect to the positive *x* axis (in each image plane) was then calculated for each image, with subsequent measurements conditioned on the previous one to ensure consistency in axis identification. These angles were labeled as the 2D cylinder axis orientation angles θ_1 and θ_2 for High Speed Camera 1 and High Speed Camera 2, respectively, for each image. Three-dimensional cylinder positions were determined from the 2D operations described above by calibrating the two high speed cameras in 3D space. Both cameras were first calibrated by simultaneously taking an image of three evenly spaced transparent calibration plates as shown in Figure 21 in Appendix B. Each plate was spaced 50 mm apart and had a grid of points spaced 20 mm apart [64]. Forty eight points in both camera snapshots were used to map the image plane of each camera to the 3D global space using a Direct Linear Transformation (DLT) [65]. An example of this mapping mechanism is shown in Figure 7, where the global spatial location of a point $[x_c, y_c, z_c]$ is mapped to the pixel location $[x_{c1},\ y_{c1}]$ on the image plane of High Speed Camera 1 and pixel location $[x_{c2}, y_{c2}]$ on the

image plane of High Speed Camera 2. Camera distortion errors were assumed be negligible for the imaging system used in these experiments and were thus neglected in this calibration.

The spatial calibration was used to find 22 DLT coefficients, which can be used for mapping pixel location from the 2 cameras into global space. Using these coefficients, four linear equations were constructed using the relationships provided by [65] relating the cylinder centroid locations in each camera's image plane ($[x_{c1}, y_{c1}, x_{c2}, y_{c2}]$) to its actual centroid location in global space ($[x_c, y_c, z_c]$). The equations were solved iteratively to find the global centroid location $[x_c, y_c, z_c]$ from the DLT parameters as described by [65]. For numerical stability, an initial guess of [1 cm, 1 cm, 1 cm] was used before the iterative process converged to values with less than a 0.001 cm difference from the previous iteration. These steps were repeated for each set of images to calculate the three-dimensional centroid locations for each cylinder as a function of time. Using these data, the 3D velocity components ($[u, v, \text{and } w]$) could then be determined as positional derivatives.

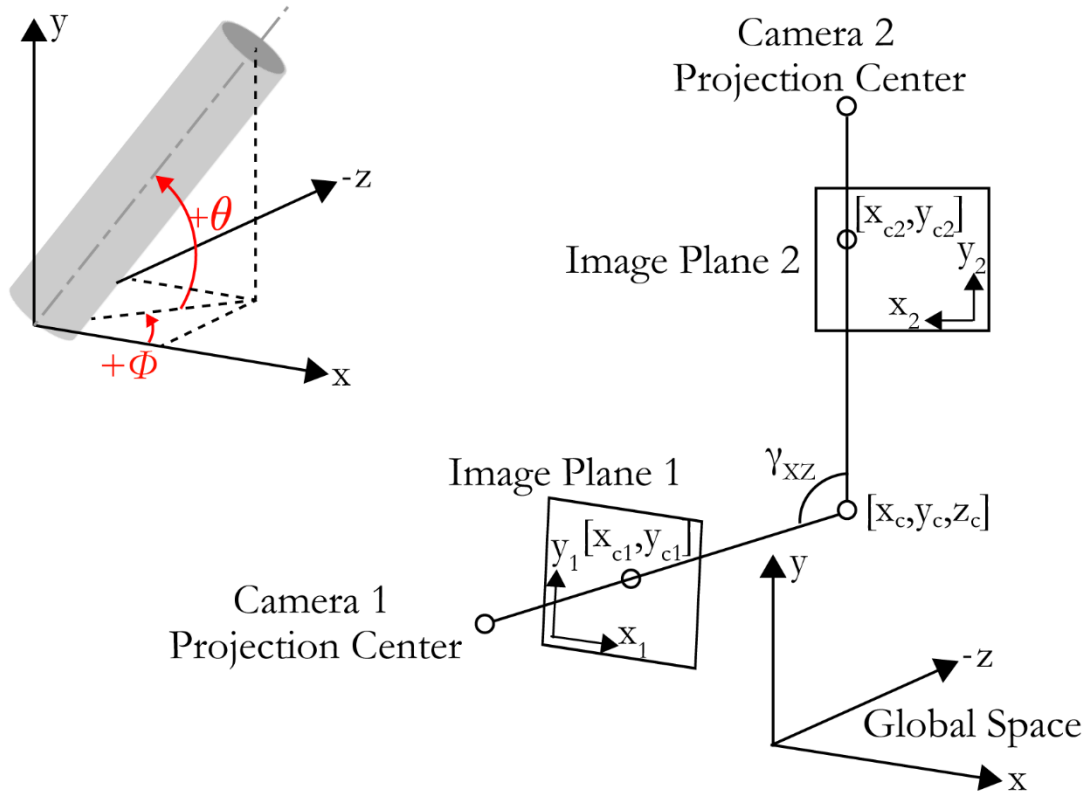

Figure 7. Schematic drawing of the camera orientation and calculation of position in global space from the two camera images. A known set of global spatial points was measured in pixel locations in both High Speed Cameras, enabling the calculation of Direct Linear Transform coefficients, which were used to calculate 3D positions of the centroid of each falling cylinder in global space.

For each cylinder, the 2D High Speed Camera 1 orientation angle (θ_1) values were used to represent the 3D orientation angle (θ) values. The cylinders' axes of symmetry were nearly perpendicular to High Speed Camera 1 at all times, therefore the projection of the cylinder in the 2D plane is an accurate representation of the orientation angle θ.

Calculation of the azimuthal angle (Φ) relied only on the major cylinder axis length in each high speed camera view. A cylinder oriented with $\Phi = 0$ will have a major axis length equal to the cylinder length (L_c) as viewed from High Speed Camera 1. According to Equation (14), as the cylinder turns toward or away from this camera, the apparent length of the major axis will initially increase before decreasing to the length of the cylinder diameter (D_c) where $\Phi = \pm 90°$. We see that

$$L_R = L_C \cos(\Phi) + D_C \sin(\Phi), \quad (14)$$

where L_R is the projected or apparent major axis length for the cylinder and Φ is the azimuthal angle of the cylinder defined from the positive x-axis in the $x - z$ plane, as indicated in Figure 4. The azimuthal angle coordinate system is discussed in more detail in Appendix B, along with plots of the angle possibilities for each aspect ratio cylinder (see Figure 24). Since there are often two possible angles which map to a measured length L_R, the projected major axis length from High Speed Camera 2 was used to identify the correct azimuthal angle for each cylinder. These calculations were repeated for each time-step to resolve variations in cylinder orientation as a function of time.

Chapter 3: Results and Statistical Analysis

3.1 Cylinder landing sites, trajectories and orientations

Figure 8 shows the landing sites for the UD cylinders (top row) and CD cylinders (bottom row) for each aspect ratio. Each point in the plot is the landing site of an individual cylinder. The rings represent radial distance from the center, while the overlaid angular histogram plot shows the percentage of cylinders landing in 20º angular bins of the landing site target. Overall, the landing sites of the UD cylinder classes were distributed relatively uniformly around the center of the target, clustered tightly around $r = 0$ cm. For cylinders with AR of 2 and 4, the UD cylinders tended to group in a tighter circle around the center of the target than the AR = 1 UD cylinders. In contrast, the CD cylinders tended to land on the left-hand side of the target, where the denser end of the cylinder was initially oriented. For $AR = 1$ CD cylinders (Figure 8D), the majority of the landing sites were located close to $r = 0$ cm; however, a majority of the cylinders still landed slightly towards the left-hand side of the target, as shown by the overlaid histogram. At the most extreme aspect ratio ($AR = 4$), every cylinder (Figure 8F) drifted far to the left before impacting the target at approximately $r = 18$ cm. The landing sites for the CD cylinders with $AR = 2$ (Figure 8E) were scattered throughout the left hand side of the landing site target, with radial distances ranging from $r = 2$ cm to $r = 23$ cm. Landing sites for this case were not grouped at one particular radial location. Some of the landing sites were similar to those of the $AR = 1$ CD cylinders (close to $r = 0$ cm) and some were similar to those of the $AR = 4$ CD cylinders (around $r = 20$ cm), with a wide distribution of landing sites in between. It is apparent from the landing sites shown in Figure 8 that altering the density distribution and AR of a cylinder has a large influence on where it settles. To explain this variation, the settling behavior of each cylinder is further investigated below.

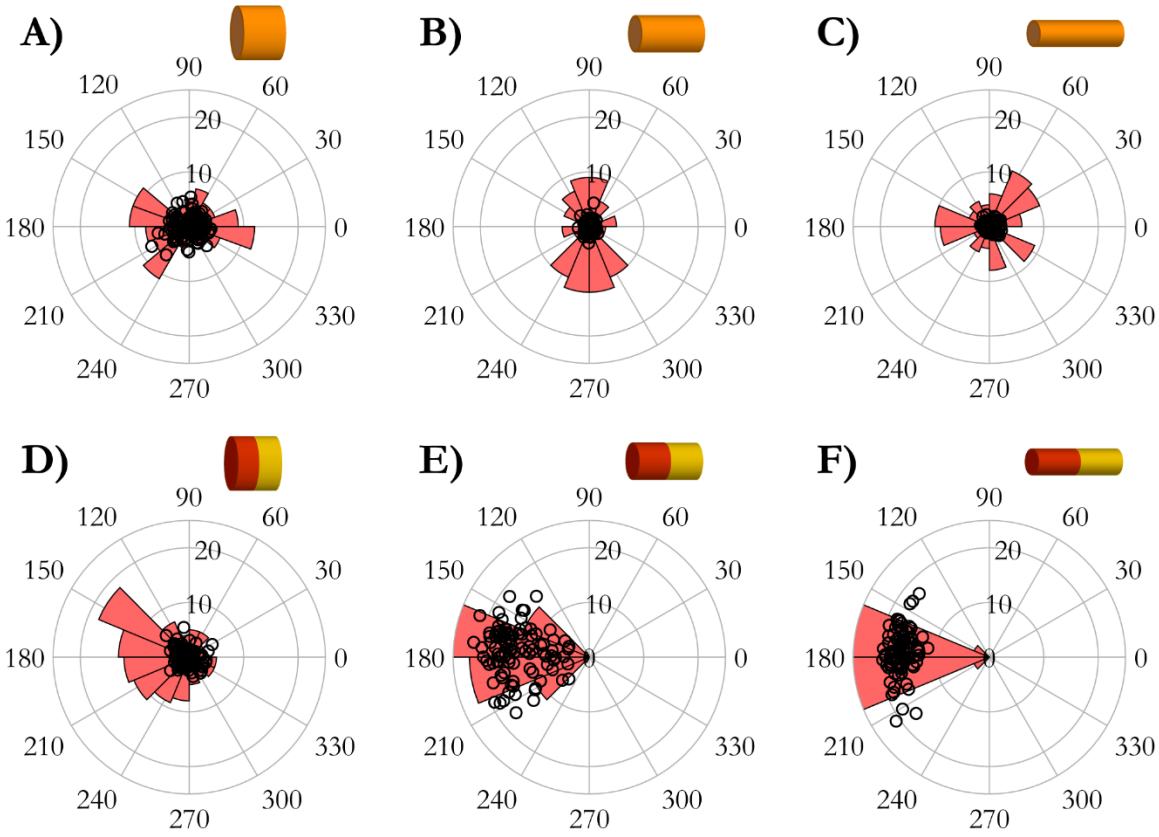

Figure 8. Landing sites of each of six cylinder classes (black circles), together with angular histogram (18 evenly spaced transparent red wedges, each representing a bin of 20°). Outer edge of histogram shows angles marked in degrees; rings represent radial distance in cm as well as number of cylinders in each bin (extends beyond the bounds of the plot in (E) and (F)).

To further quantify settling behavior, we tracked cylinder centroid locations (x_c, y_c, z_c) and orientations (θ, Φ) over time, as described in Chapter 2. Figure 9 displays the centroid location of each $AR = 1$ cylinder as it settled through the field of view, projected onto the $x - y$ (side view) and $x - z$ (top view) planes. Despite minor variation, both classes of $AR = 1$ cylinders fell with similar trajectories, with centroid positions showing little variance in x and z within each trajectory; across multiple trajectories, centroid position ranged from -4 cm to 4 cm in both the x and z coordinates. Qualitatively, the $AR = 1$ UD cylinders (Figure 9A and C) showed slightly higher variance in both lateral directions, with slightly greater side-to-side and in-and-out-of-plane motion compared to the CD cylinders. This can be observed by the slight waviness in the cylinder

tracks shown in Figure 9A compared to the straighter tracks in Figure 9B, and by the longer tracks in Figure 9C compared to shorter ones in Figure 9D.

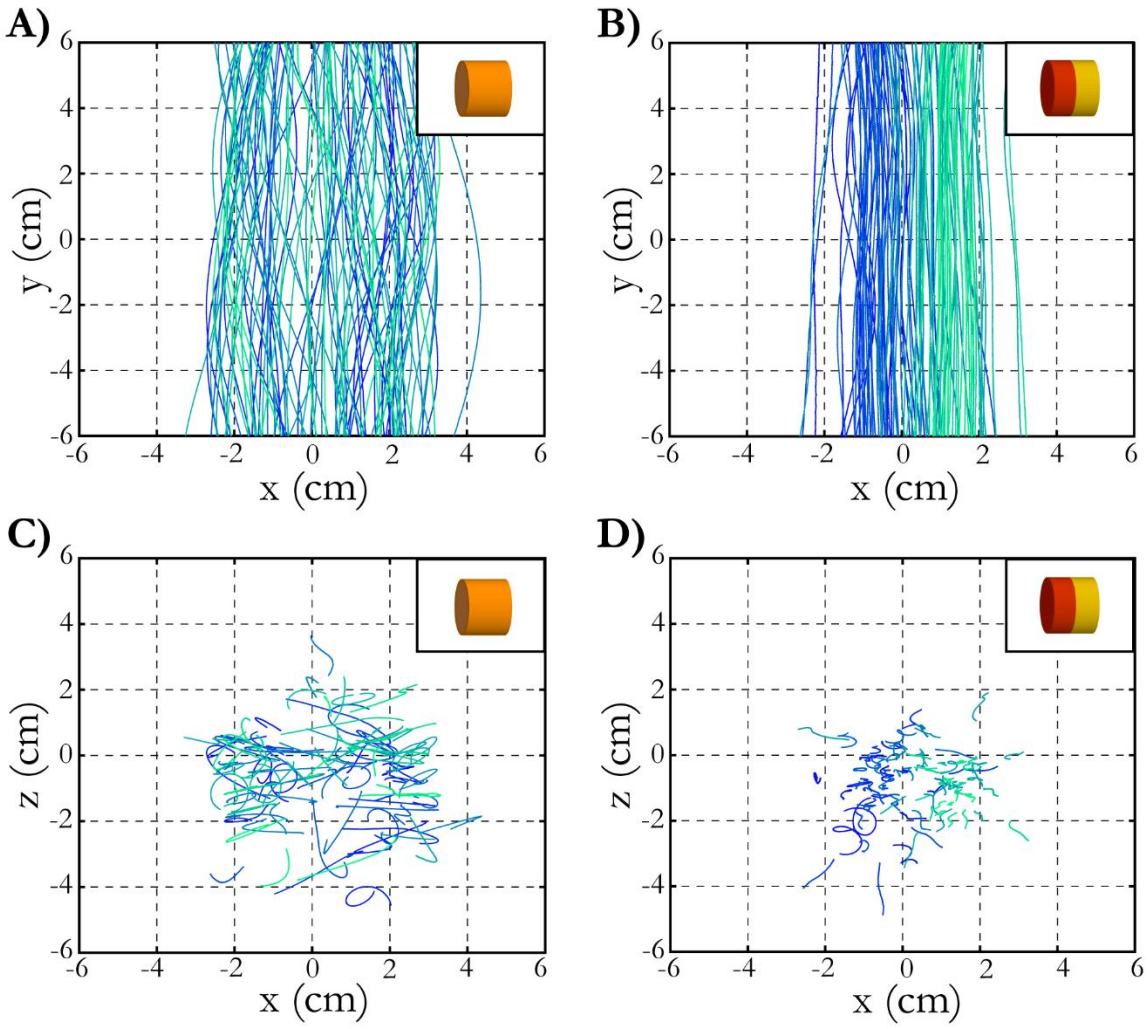

Figure 9. Trajectories for both classes of $AR = 1$ cylinders in the $x - y$ plane and $x - z$ plane. (A,C) UD cylinders (B,D) CD cylinders. Trajectory color variation was used to separate the different trials for clarity in visualization.

Figure 10 shows the orientation of the principal axis of each cylinder throughout the field of view for both $AR = 1$ cylinder classes. Here, we can see a variety of motion for the UD class: cylinders did not display a constant fall orientation, and the orientation varied periodically in the range of $\theta = -65°$ to $150°$ (with some cylinders having larger oscillations in θ than others). It appears that the axis of symmetry of the UD cylinders oscillated about either a horizontal position

($\theta = 0°$) or a vertical position ($\theta = 90°$). Periodicity was also present for some CD cylinders, but with much smaller-amplitude oscillations in θ. Despite the similarities in settling trajectories as shown in Figure 9, the bimodality in θ of the two different classes of $AR = 1$ cylinders during settling suggest that they had two distinct settling behaviors.

Cylinders typically settle with a preferred orientation that maximizes their projected area in the direction of settling up to $Re_p = 100$ [14]. It is therefore unsurprising that the $AR = 1$ UD cylinders did not display a single preferred fall orientation, given that the minimum projected area of a vertical $AR = 1$ cylinder (that is, the axis of symmetry in a vertical position) is only 24% less than the projected area for the same cylinder with the axis of symmetry in a horizontal position. For comparison, a cylinder with $AR = 2$ sees a difference of 87% between the minimum and maximum projected areas, and is likely to fall with its principle axis horizontal to maximize the projected area. In contrast to $AR = 1$ UD cylinders, the orientation of the $AR = 1$ CD cylinders was very consistent at approximately $\theta = 90°$, indicating a primarily vertical cylinder orientation (with small oscillations in some cases). This result indicates that the CD cylinders rotated 90º after being released from the dropping mechanism, so that the denser end of the cylinder pointed downward. Inertia may be responsible for a small overshoot of the vertical position, which then results in a gentle oscillation due to the presence of restoring torques. Some of the UD cylinders behaved similarly, while other UD cylinders oscillated around $\theta = 0°$ as stated above.

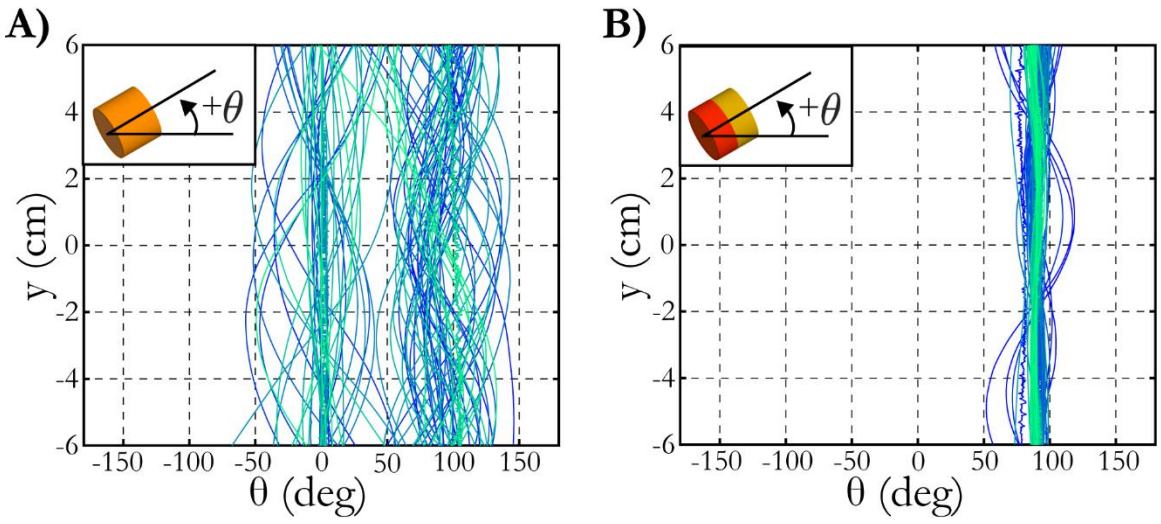

Figure 10. Major axis orientation for all trials of both $AR = 1$ cylinder classes. (A) UD cylinders (B) CD cylinders.

The centroid tracking results for $AR = 2$ cylinders are shown in Figure 11. Here, the UD and CD cylinders displayed different settling behaviors, as we observed in the $AR = 1$ classes. However, the CD cylinders fell with two distinctly different behaviors within the same class, with some cylinders falling at a shallow steady angle and others oscillating about a vertical orientation. For the UD class (Figure 11A), the cylinders remained in the center of the field of view and fell with a straight trajectory with minimal movement in the lateral directions. In contrast, most of the CD cylinders drifted in the direction of the denser cylinder end, with an overall range between $x = -2$ cm and $x = -13$ cm. The resulting trajectory for these drifting cylinders appeared straight, but slanted, in the $x - y$ plane. The slight bias in the trajectories towards the negative z direction (shown in Figure 11D) was due to the dropping mechanism being angled with respect to our coordinate system by 5° in the $+\Phi$ direction. We found that some of the CD cylinders had oscillating trajectories and had a smaller x_{range} than the cylinders with slanted trajectories, where the x_{range} represents the distance each cylinder traveled in the x-direction in the global space. A bigger distinction between the two classes can be observed by comparing the cylinder orientations in Figure 12. For the UD class (Figure 12A), the cylinders maintained steady orientations around $\theta =$

0 (cylinder principal axis was horizontal). This behavior was very different from either of the two behaviors observed for the CD class (Figure 12B). Here, 71 of the $AR = 2$ CD cylinders (74%) held a constant orientation angle around $\theta = 19°$ throughout the entire field of view, and drifted to the left side throughout the observed period. A second, smaller group of eighteen $AR = 2$ CD cylinders rotated $90°$ after being released from the dropping mechanism, after which they fell vertically. This is the same mode present in all the $AR = 1$ CD cylinders—that is, the cylinder falls with its principal axis vertical and oscillates around this orientation. The vertically falling $AR = 2$ CD cylinders showed oscillatory motion with greater amplitude than the $AR = 1$ CD cylinders, but similar behavior otherwise. A third group of seven $AR = 2$ CD cylinders appeared to be transitioning between these two modes, with their initially slanted trajectories becoming curved towards the end of the measurement domain.

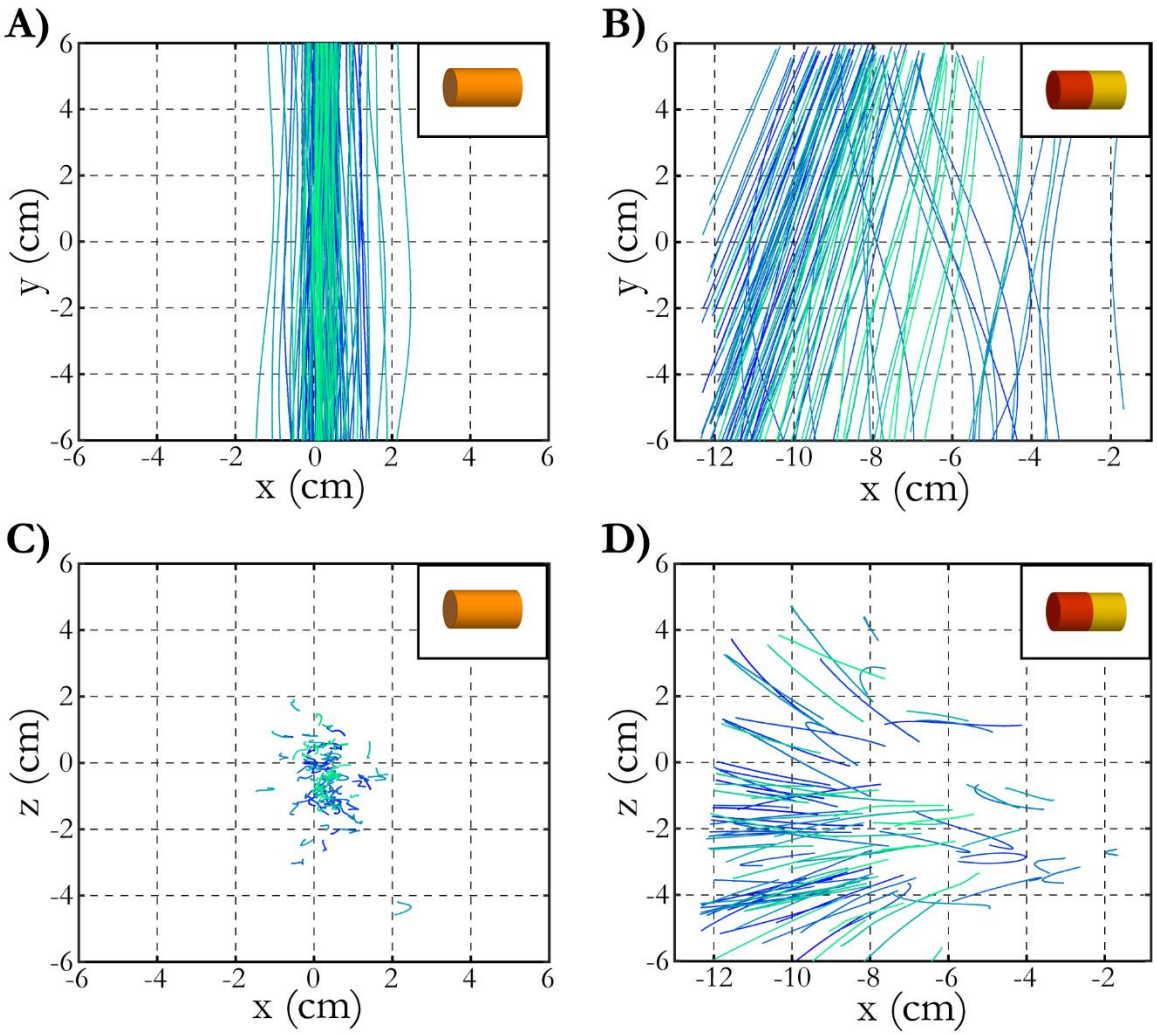

Figure 11. Trajectories for both classes of $AR = 2$ cylinders in the $x - y$ plane and $x - z$ plane. (A,C) UD cylinders (B,D) CD cylinders. The x-axis was shifted 7 cm to the left for the CD cylinders to account for the horizontal drift upon release; the field of view was changed so that more cylinder motion was observable.

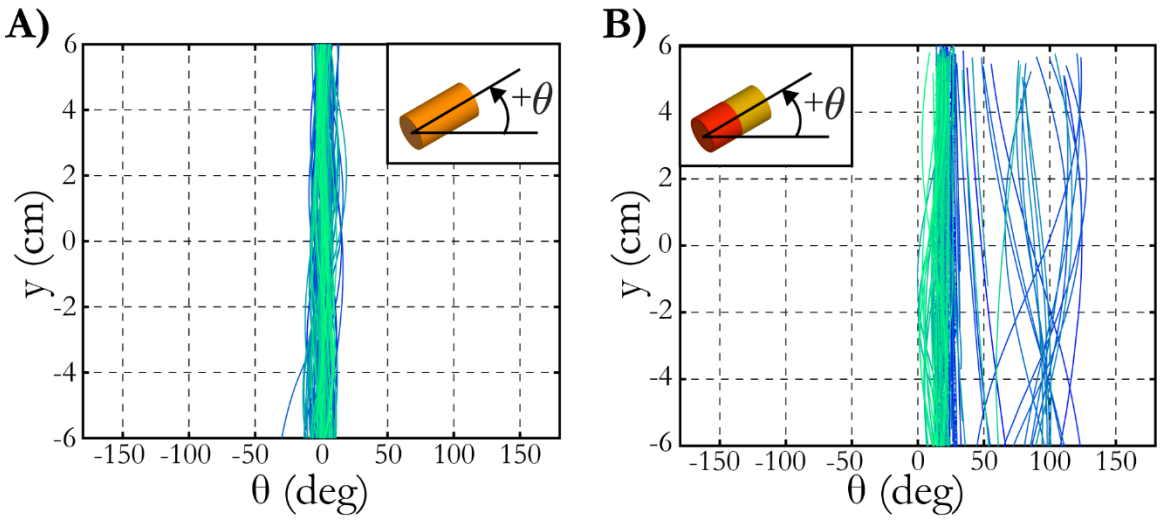

Figure 12. Major axis orientation for all trials of both $AR = 2$ cylinder classes. (A) UD cylinders (B) CD cylinders.

Figure 13 shows the trajectories for the $AR = 4$ cylinders. The UD cylinders (Figure 13A and C) settled with a straight trajectory, with very little variance in the lateral directions. In contrast, the CD cylinders (Figure 13B and D) fell with slanted trajectories, similar to the larger portion of $AR = 2$ CD cylinders described above. The trajectories for these cylinders in Figure 13D were once again not evenly distributed around the $z = 0$ direction (see Figure 13D) due to the dropping mechanism being angled 5° in the Φ direction. Unlike the $AR = 2$ CD cylinders, the $AR = 4$ CD cylinders did not display a multi-modal settling behavior. All 100 cylinders showed a consistent slanted trajectory, as shown in Figure 13B.

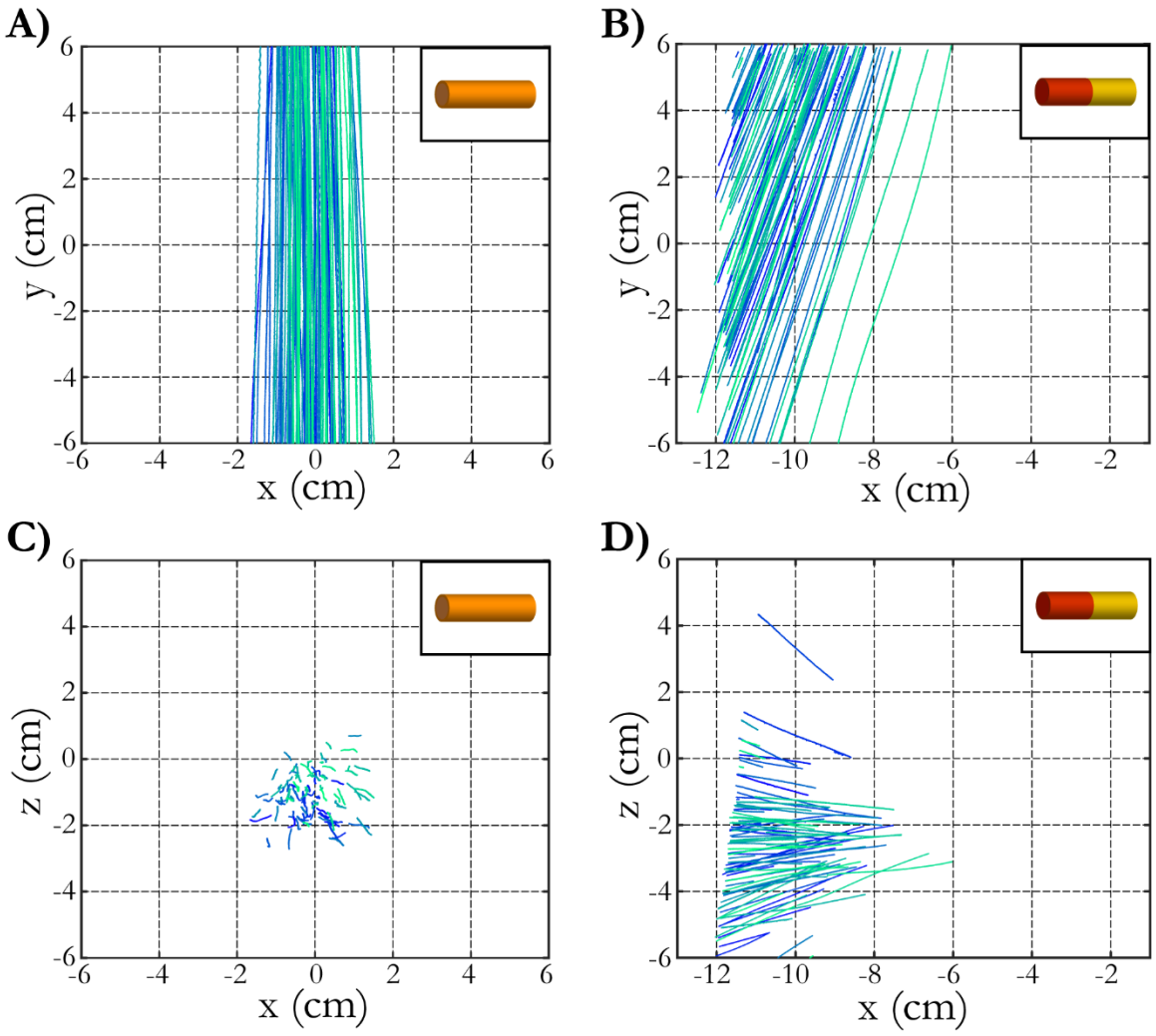

Figure 13. Trajectories for both classes of $AR = 4$ cylinders in the $x - y$ plane and $x - z$ plane. (A,C) UD cylinders (B,D) CD cylinders. The x-axis was shifted 7 cm to the left for the CD cylinders to account for the horizontal drift upon release, which allowed us to change the field of view so that more cylinder motion was observed.

Figure 14 shows very consistent cylinder orientations at approximately zero degrees for all $AR = 4$ UD cylinders. The major axis of these cylinders remained perpendicular to the settling direction throughout the entire trajectory. The $AR = 4$ CD cylinders had a constant slanted orientation angle θ of approximately 9.5°. However, this angle is shallower than the average stable angle of the subgroup of $AR = 2$ CD cylinders with a slanted trajectory, which had a stable orientation around 19°.

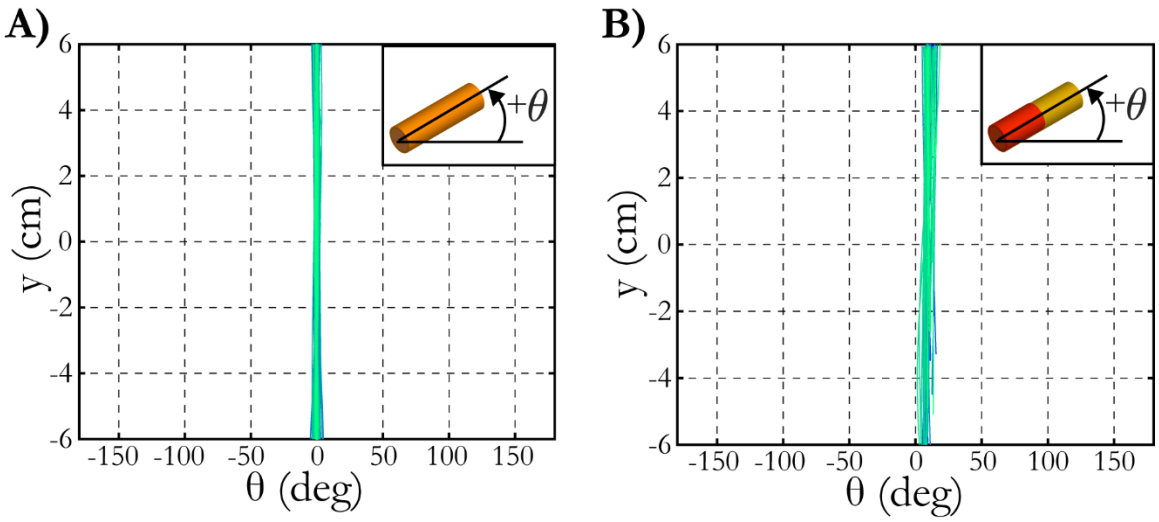

Figure 14. Major axis orientation for all trials of both $AR = 4$ cylinder classes. (A) UD cylinders (B) CD cylinders.

3.2 Cylinder Velocities

To gain further insight into the behavior of the six classes of cylinders, we plotted the average vertical velocity $\bar{v}$ for each class (shown in Figure 15). Because of their interesting mixture of settling behaviors, the $AR = 2$ CD cylinders were separated into three different groups prior to the velocity calculations. The groups were based upon cylinder orientation θ throughout the field of view. Any $AR = 2$ CD cylinder trial with a maximum cylinder orientation angle θ of less than 35° ($\theta_{max} < 35$) was considered to be in group 1. Here, 71 cylinders with $\theta_{max} < 35$ were visually confirmed to be the same 71 cylinders with a slanted trajectory in Figure 11B. Group 1 is represented with a cartoon of a slanted-trajectory cylinder in the horizontal axes of Figure 15 and Figure 16. A second group of cylinders was identified as having a maximum orientation angle between 35° and 75° ($35 \leq \theta_{max} < 75$). This second group only contained seven cylinder trials and was therefore omitted from this section; however, this group was visually confirmed to be the "transition" group, which fell stably with slanted trajectories but appeared to transition or "turn" at the end of the observation period. The third group of $AR = 2$ CD cylinders was defined as all

cylinder trials with $\theta_{max} \geq 75$. Here, eighteen cylinder trials of $AR = 2$ CD cylinders were included, visually confirmed to be the same eighteen trials with a vertical-oscillating orientation in Figure 11B. This separation of $AR = 2$ CD cylinders based on θ_{max} results in a total of seven different cylinder classes (including all aspect ratios and density distributions, with $AR = 2$ divided into three classes instead of two). Figure 15 shows that the $AR = 2$ CD cylinders in group 2 (with a primarily vertical orientation and oscillating trajectories) fell with the greatest magnitude of vertical velocity, while the $AR = 1$ CD cylinders, which also fell with vertical orientations and oscillating trajectories, had the second-greatest vertical velocity magnitude. For the remainder of the classes, the cylinders with the smallest projected area in the vertical direction fell fastest and the cylinders with the largest projected area fell slowest. We note that the cylinders which fell in a stable, slanted orientation ($AR = 2$ CD group 1 and $AR = 4$ CD) fell more slowly than their UD counterparts, but had a nontrivial lateral velocity.

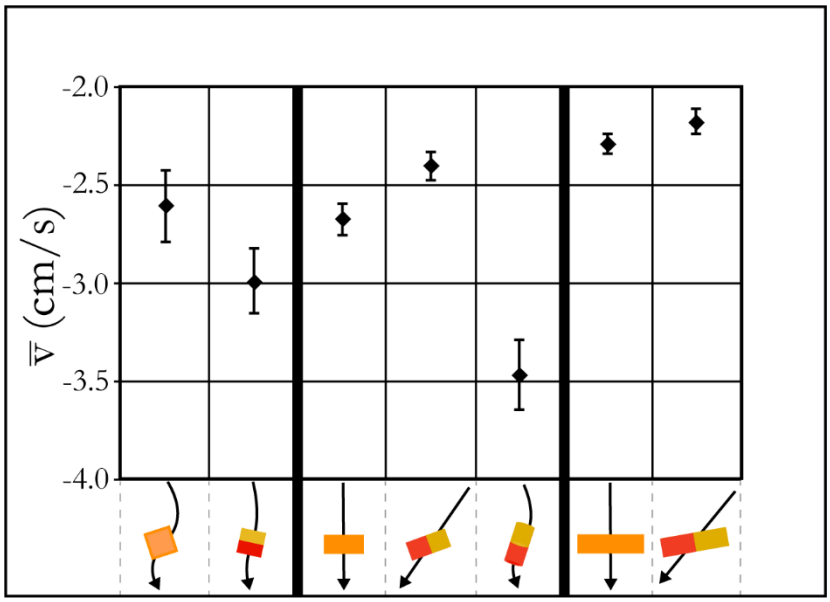

Figure 15. Average vertical velocities for the seven cylinder classes (two groups are present for the $AR = 2$ CD cylinders, separated by maximum cylinder orientation angle). The error bars represent one standard deviation.

Additionally, $\bar{u}$ and $\overline{w}$ were plotted for each of the classes (shown in Figure 16). The cylinders that fell with a slanted trajectory had the highest-in-magnitude horizontal velocity of $\bar{u} \approx$

0.6 cm/s in both classes. The $AR = 2$ CD cylinders that fell with oscillating vertical trajectories had a large standard deviation in horizontal velocity, which was a result of the cylinders accelerating and decelerating throughout the vertical oscillatory motion; however, the average $\bar{u}$ remained close to zero. This was also true for $\bar{w}$; all cylinder classes had minimal velocity in the z direction. The two classes with the largest-in-magnitude $\bar{w}$ were the cylinders settling with a constant slanted orientation ($AR = 2$ CD group 1 and $AR = 4$ CD).

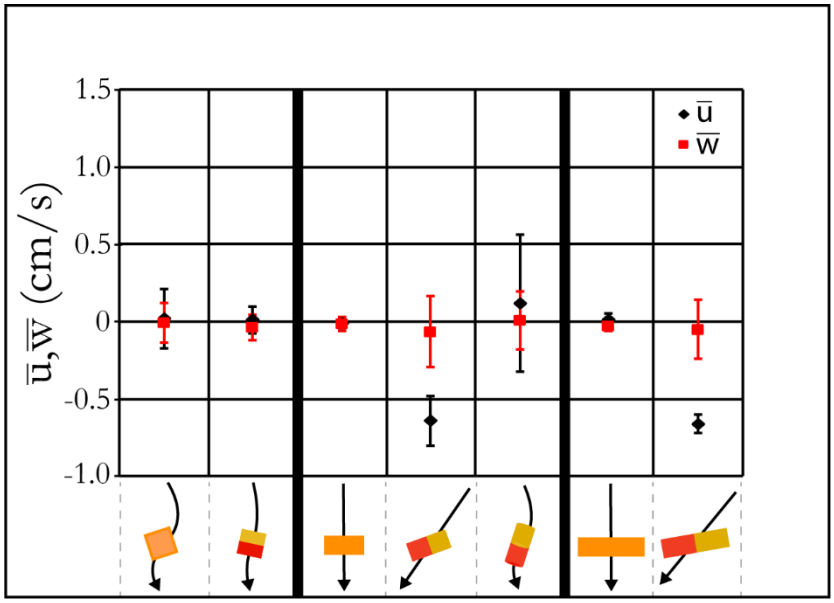

Figure 16. Average u and w velocities for the seven cylinder classes (two groups are present for the AR = 2 CD cylinders, separated by maximum cylinder orientation angle). The error bars represent one standard deviation.

3.3 Statistical significance testing

A more detailed statistical analysis was performed within each cylinder AR class to quantify the significance of the effect of density distribution on settling behavior by comparing the mean values and distributions using an unpaired t-test. We chose to test with a 95% significance level, meaning that if the *t*-value calculated between a pair of independent variables was between

$-t_{95}$ and t_{95}, no significance was recorded. In this case, the two independent variables were relevant behavioral measurements, such as average vertical velocity, from two cylinder classes (the UD and CD cases for a given aspect ratio). Here, $t_{95} = 1.98$, where $n = 200$ (total trials between the two tested classes) was used to look up the appropriate t_{95} value in a t-value table. The t_{95} value is treated identically to the upper and lower bounds on a 95% significance level z-test. Equation (15) shows the equation used in all t-test comparisons,

$$t = \frac{\bar{x}_1 + \bar{x}_2}{\sqrt{\frac{(n_1-1){s_1}^2+(n_2-1){s_2}^2}{(n_1-1)+(n_2-1)}(\frac{1}{n_1}+\frac{1}{n_2})}}, \tag{15}$$

where $\bar{x}_1$ and $\bar{x}_2$ are the average parameters being tested from sample classes 1 and 2 respectively, s_1 and s_2 are the sample standard deviations from the two classes, and n_1 and n_2 are the number of cylinder trials from the two classes. Table 1 shows the average of each tested variable for a given class along with the significance results. All boxes filled in green mean that the variable between the two test classes was at least 95% significantly different. Here, t-tests were only performed between UD and CD cylinders within each aspect ratio, not across aspect ratios. The $AR = 2$ cylinders have two different class pairs for comparison, given the different behaviors mentioned in Section 3.1 Cylinder landing sites, trajectories and . It was necessary to test the $AR = 2$ UD class vs. each of the two $AR = 2$ CD cylinder groups due to the bimodality of the settling behaviors shown in this class.

When comparing the average vertical velocity ($\bar{v}$) between UD and CD cylinders of the same aspect ratio, we can see that there was a significant difference between all four classes being compared. When comparing the average horizontal velocity ($\bar{u}$) between UD and CD cylinders, only the $AR = 1$ cylinders did not show a difference at the 95% significance level. Fewer significant differences were observed in the other horizontal velocity component; the $AR = 2$ UD cylinders and $AR = 2$ CD cylinders with slanted trajectories are the only classes that showed a significant difference in $\bar{w}$ velocities.

	No Significant Difference
	95% Significant Difference

Table 1. Unpaired t-test results between same AR cylinder classes.

Test Variable	AR=1 UD AR=1 CD	AR=2 UD AR=2 CD Slanted	AR=2 UD AR=2 CD Oscillatory	AR=4 UD AR=4 CD
$\bar{u}$ (cm/s)	2.04×10^{-2} 1.21×10^{-2}	-6.80×10^{-3} -6.37×10^{-1}	-6.80×10^{-3} 1.18×10^{-1}	1.67×10^{-2} -6.60×10^{-1}
$\bar{v}$ (cm/s)	-2.61 -2.99	-2.67 -2.40	-2.67 -3.47	-2.29 -2.18
$\bar{w}$ (cm/s)	-7.00×10^{-3} -3.60×10^{-1}	-1.42×10^{-2} -6.57×10^{-2}	-1.42×10^{-2} 8.00×10^{-3}	-3.01×10^{-2} -5.10×10^{-2}
σ_u (cm)	3.40×10^{-1} 1.35×10^{-2}	8.72×10^{-2} 5.29×10^{-2}	8.72×10^{-2} 4.64×10^{-1}	1.78×10^{-2} 2.50×10^{-2}
σ_v (cm)	1.02×10^{-1} 4.24×10^{-2}	2.79×10^{-2} 2.82×10^{-2}	2.79×10^{-2} 1.82×10^{-1}	1.51×10^{-2} 1.73×10^{-2}
σ_w (cm)	1.96×10^{-1} 8.19×10^{-2}	4.80×10^{-2} 3.16×10^{-2}	4.80×10^{-2} 1.59×10^{-1}	2.52×10^{-2} 2.53×10^{-2}
σ_θ (deg)	20.4 4.41	5.00 2.77	5.00 15.9	8.39×10^{-1} 8.63×10^{-1}
σ_Φ (deg)	2.76 1.39	1.46 2.69	1.46 2.68	1.30 1.53
x_{range} (cm)	1.17 3.62×10^{-1}	2.55×10^{-1} 2.91	2.55×10^{-1} 1.73	1.75×10^{-1} 2.13
z_{range} (cm)	6.94×10^{-1} 3.23×10^{-1}	2.10×10^{-1} 9.09×10^{-1}	2.10×10^{-1} 6.36×10^{-1}	2.08×10^{-1} 5.26×10^{-1}

Significant difference was present in the standard deviation of u (that is, σ_u) for all classes, where σ_u is the standard deviation of u for a single trajectory and the t-test measures the difference in the average σ_u of two different classes. Although $\bar{u}$ was not significantly different between the $AR = 1$ cylinder classes, a significantly different standard σ_u is a result of the variation in u for the $AR = 1$ CD cylinders with vertical oscillatory motion (that is, the $AR = 1$ CD cylinder trajectories

showed larger "excursions" in x, and a correspondingly higher variation in u). This significant difference in σ_u persists across all tested class pairs. Additionally, significant differences were found in the standard deviation of v (σ_v) between both $AR = 1$ classes as well as the $AR = 2$ UD cylinders and $AR = 2$ CD oscillating classes. A significant difference between classes in the standard deviation of *w* occurs between each pair other than the AR = 4 cylinder classes. The next two variables displayed in the table are the standard deviations of θ and Φ for each class. The $AR = 4$ cylinders were the only pair that did not show significant difference between the standard deviations of θ and Φ. All cylinder classes showed a significant difference in their x_{range} and z_{range}. This result directly relates to the difference between the straight or nearly-straight trajectories of the AR = 1 CD, AR = 2 UD, and AR = 4 UD cylinders and the slanted or oscillating trajectories of the AR = 1 UD, AR = 2 CD and AR = 4 CD cylinders (described in Section 3.1).

3.4 PIV Vorticity Analysis

PIV experiments were performed to clarify the influence of the wake structures behind the settling cylinders on the different cylinder behaviors. Figure 17 shows contours of out-of-plane vorticity ω_z for three distinct settling behaviors. The first behavior, in which cylinders fell straight down with no change in orientation angle, is typified by the $AR = 4$ UD cylinders (Figure 17A). Symmetric vortex rings behind the cylinder, identified by the regions of opposite-signed vorticity located behind each end of the cylinder, appear to have been shed at regular intervals as the cylinder settled through the water. These vortex rings detached periodically and decreased in strength over time after being shed from the cylinder. It is likely the $AR = 2$ UD cylinders, which also fell with a similar stable horizontal orientation, had similar wake structures.

The second behavior, in which cylinders fall at a fixed angle with a slanted trajectory (but with little to no oscillation), is typified by the $AR = 4$ CD cylinders. An example is shown in Figure 17B. On the top leading edge of the cylinder, a region of positive vorticity, likely caused by an attached vortex, remained present and attached as the cylinder passed through the measurement domain. A second region of interest is located behind the trailing edge of the cylinder, where we observed two patches of opposite-signed vorticity. However, the positive vorticity in this pair is weaker (1.5 s^{-1}) than the negative vorticity (2.5 s^{-1}). We hypothesize that the positive vorticity is less defined at the upper trailing edge because the strong attached vortex on the leading edge previously influenced the flow where the upper trailing edge is located in the figure, leading to a noisy background flow. Some evidence of vortex shedding can be seen in the trailing-edge region of negative vorticity; this may also be present in the trailing-edge positive vorticity, but is not visible due to the noisy background created by the attached leading-edge vortex.

The third behavior, in which cylinders fall in a primarily vertical orientation with some periodicity in their trajectory and orientation, is represented by the $AR = 1$ CD cylinder (Figure 17C). This cylinder shed several pairs of vortices as it settled. The vortex pairs were shed at the three locations where the cylinder changed directions over the course of its periodic trajectory through the field of view (specifically, these vortex structures can be seen at the locations $x = -3$ and $y = 5$, $x = -1$ and $y = 0$, and $x = -1.9$ and $y = -3.8$ cm. From this, we can conclude that a pair of vortices are shed every time a cylinder with an oscillatory trajectory cylinder changes direction in free fall. We note that the vorticity for the $AR = 1$ CD cylinder is relatively weak when compared to the other two larger AR cylinders due to the smaller cylinder dimensions, which leads to shear stresses (and vorticity) which are smaller in magnitude.

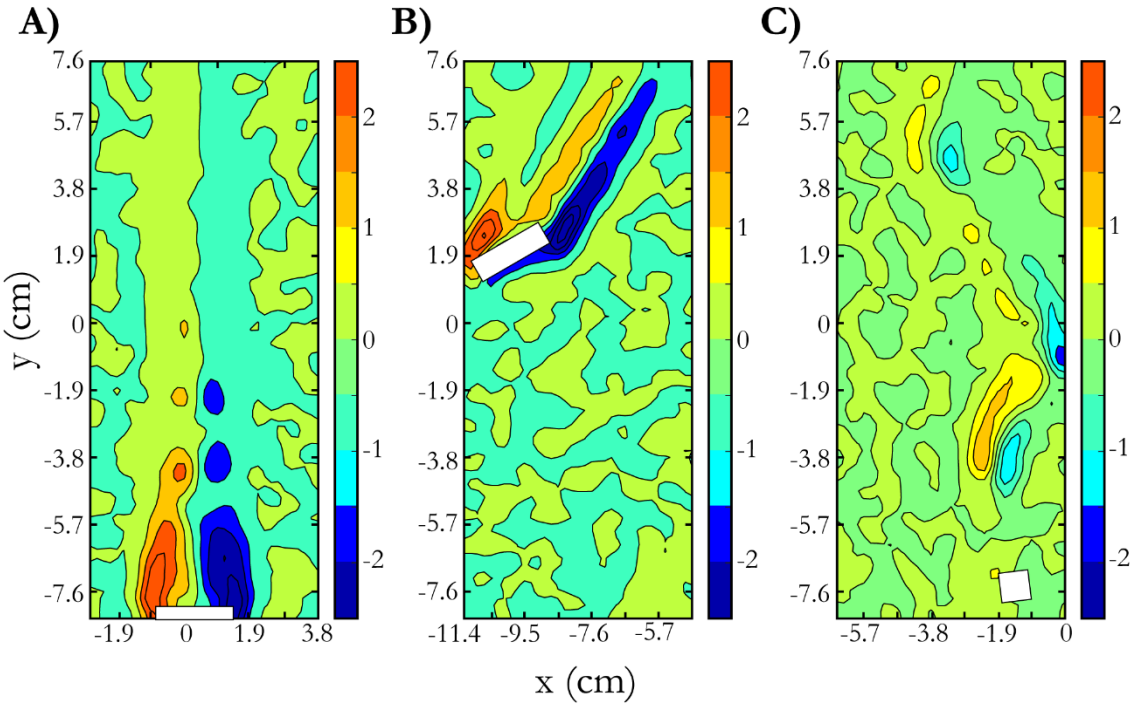

Figure 17. Contour plots of out-of-plane vorticity ω_z (s^{-1}) for cylinder classes falling with different settling behaviors, showing (A) $AR = 4$ UD cylinder, (B) $AR = 4$ CD cylinder, and (C) $AR = 1$ CD cylinder.

Chapter 4: Discussion

In the previous section, we have described different behaviors of falling cylinders. Here, we formally group the behaviors of all measured cylinders into three different modes:

(0) vertical trajectory, horizontal orientation

(1) slanted trajectory, stable angled orientation

(2) vertical trajectory, oscillating orientation

Uniform density cylinders with $AR = 2$ and $AR = 4$ display Mode 0 behavior. Compound density cylinders with $AR = 4$ display Mode 1 behavior, and compound density cylinders with $AR = 1$ display Mode 2 behavior. Some $AR = 1$ UD cylinders display a variation of Mode 0 behavior (in which the cylinder orientation oscillates around a horizontal position and the trajectory displays some periodicity), while other cylinders in the same class display Mode 2 behavior. As previously discussed in Section 3.1 Cylinder landing sites, trajectories and , the numerous settling behaviors are likely due to the small difference in projected area between a vertically and horizontally oriented $AR = 1$ cylinder, so that neither mode is dominant. Unlike the $AR = 2$ CD cylinders, the two modes cannot be cleanly separated by maximum orientation angle; there appears to be a relatively smooth transition between the two modes. Future work may elucidate the mechanisms which lead to a primarily-vertical orientation *vs.* a primarily-horizontal orientation in cylinders with $AR = 1$.

Within the $AR = 2$ CD cylinders, both Mode 1 and Mode 2 can be observed, and the distinction is relatively clear. A small group of transition cylinders can also be observed, transitioning from Mode 1 to Mode 2 throughout the field of view; however, this group is small, and still allows the two main groups to be distinguished *via* a threshold on the maximum orientation angle as discussed in Section 3. While some of the differences between the two main groups may be attributed to minor inconsistency in cylinder fabrication, this does not explain the significant

differences observed. The rest of this section will quantitatively separate the two different modes for the $AR = 2$ CD cylinders and explore potential reasons why both modes can exist at $Re_p \approx 210$.

To show that there is a measurable difference between the two modes present for $AR = 2$ CD cylinders, we present the time-resolved vertical velocity for each cylinder, after they have been grouped by thresholds on the maximum cylinder orientation angle achieved in a single trial. Figure 18A shows all $AR = 2$ CD cylinders with a maximum cylinder orientation angle during free fall of less than 35° ($\theta_{max} < 35$). This group has vertical velocity magnitudes ranging from 2.2 to 2.6 cm/s. These are the same cylinders associated with the slanted trajectories previously discussed in Figure 11 (which we have now classified as Mode 1). The quantitative distinction of the orientation angle threshold allowed us to separate the trajectories with the qualitative features of Mode 1 behavior, and to calculate their vertical velocities separately from the rest of the $AR = 2$ CD cylinders.

Figure 18B shows the time-resolved vertical velocity of all $AR = 2$ CD cylinders with a maximum orientation angle between 35° and 75° ($35 \leq \theta_{max} < 75$). The vertical velocities for this group are initially similar to those of the Mode 1 cylinders shown in Figure 18A. However, over time, the vertical velocities begin to increase in magnitude. The corresponding trajectories of these cylinders begin with a slanted straight line before becoming curved as the major axis of the cylinder begins to rotate toward a vertical position; however, none of the oscillation which is characteristic of Mode 2, occurs within the measurement domain. The increase in the vertical velocities of this group is likely a result of a decrease in the drag force, since the projected area becomes smaller as the cylinder major axis becomes more aligned with its own velocity vector. We will refer to this group as transitional, since they are somewhere between Mode 1 and Mode 2 (in fact, it is likely that with a larger measurement domain, we would observe these cylinders transitioning to Mode 2).

Figure 18C shows the time-resolved vertical velocities of the remaining $AR = 2$ CD cylinders where $\theta_{max} \geq 75°$. These cylinders have a much greater initial vertical velocity than the previous two groups when first entering the field of view. In this third group, vertical velocities range from approximately 2.8-3.8 cm/s. The vertical velocity appears to vary periodically for each trial in this group. Additionally, the trajectories for this group of cylinders were plotted and visually confirmed to be the oscillating centroid tracks in Figure 11. Given our observation of the transitional cylinders from this class, it is likely that this last group of cylinders spent a short time in Mode 1 before transitioning and entering the measurement domain in Mode 2.

The cross-sectional area of a cylinder which is normal to its velocity vector is a key determinant of the drag force it experiences. This projected area is a function of the angle between the cylinder's principal axis and its own velocity. For a cylinder with $AR = 2$, the projected area increases as this angle increases, up to a value of $\pm 33°$, where the area reaches its maximum. Beyond this angle, the projected area decreases. As seen from Figure 12B, the $AR = 2$ CD Mode 1 cylinders had an average orientation angle of approximately $\theta = 18°$, corresponding to a vertical projected area of 108 mm^2. This is a much larger projected area in the vertical direction than a completely vertical cylinder, which would have a vertical projected area of 38.5 mm^2. The $AR = 2$ CD Mode 2 cylinders (Figure 18C) oscillate around this vertical position, where $\theta = +90°$; while the projected area varies significantly over the cylinders' trajectories due to the periodic variation in orientation, it is on average less than the cylinders which are in Mode 1. Figure 15 verifies that the $AR = 2$ cylinders falling with a larger projected area—Mode 1, in the case of the majority of the $AR = 2$ CD cylinders; or in the case of the $AR = 2$ UD cylinders, Mode 0—have lower $\bar{v}$ velocities than do the cylinders which fell in Mode 2. The larger projected area produces more drag on the cylinder, resulting in a decrease in vertical velocity.

This same projected area analysis can be applied to the $AR = 4$ cylinder classes. The projected area for an $AR = 4$ cylinder increases as θ increases or decreases up to $\theta = \pm 16°$;

beyond this point the projected area decreases. Therefore, the $AR = 4$ cylinders oriented with $\theta = 0°$, in Mode 0 (the uniform density cylinders), with an average projected area of 144 mm^2 should have a slightly smaller average vertical velocity than the $AR = 4$, Mode 1, cylinders (the compound density cylinders), orientated at an average of $\theta = 9.5°$ with a projected area of 148 mm^2. As seen in the subgroups of the $AR = 2$ CD cylinders, the $AR = 4$ cylinders with a larger projected area have lower $\bar{v}$ velocities as shown in Figure 15.

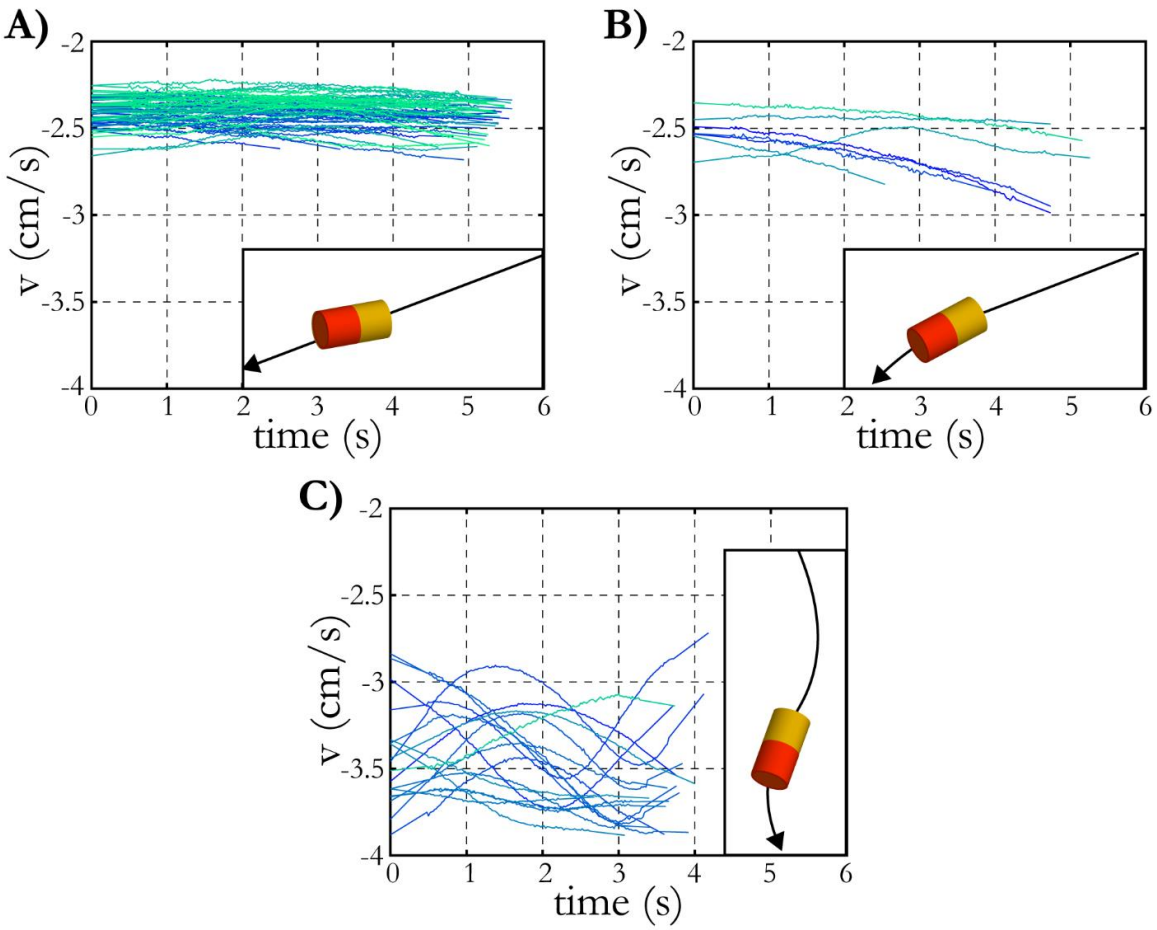

Figure 18. Velocities of each $AR = 2$ CD cylinder over time, separated by maximum orientation angle achieved during each measurement: (A) $\theta max < 35°$ (Mode 1) (B) $35° \leq \theta max < 75°$ (transitional) (C) $\theta max \geq 75°$ (Mode 2).

While it is clear that $AR = 2$ CD cylinders show both Mode 1 and Mode 2 behavior, despite reasonable consistency in fabrication and dropping method, the mechanism for transition

between Mode 1 and Mode 2 remains unclear. To further explore potential mechanisms leading to transition, we performed additional testing to independently vary Re_p while keeping cylinder size and density distribution constant. To achieve this, we varied the temperature of the water to introduce changes in the fluid density and viscosity.

First, we used ice to chill the temperature of the tank water to $1.5^{\circ}\mathrm{C}$ before dropping 28 $AR = 2$ CD cylinders using the same tank and dropping mechanism as the initial experiments. Because we were interested only in determining the qualitative cylinder behavior (mode), only one low speed camera (Sony M-IV) was used to track the trajectories of the cylinders during descent. This allowed us to observe the general character of changes in cylinder orientation, but did not allow us to quantitatively measure the vertical velocity or cylinder orientation. In this cold-water experiment, 26 of the 28 cylinders fell in Mode 1, while two cylinders showed a transitional behavior.

A second test used two 1000 W submersible circulation heaters to heat the water to $36.5^{\circ}\mathrm{C}$ before dropping 27 $AR = 2$ CD cylinders. Here, all 27 cylinders displayed Mode 2 behavior. Vertical velocities were not measured quantitatively, but were observed to be equal to or larger than the vertical velocities of the same cylinders at room temperature ($20^{\circ}\mathrm{C}$) measured during the initial experiments. This observation, together with the decrease in the kinematic viscosity of the water in the hot-water experiment, allows us to assume that the average Reynolds number of the $AR = 2$ CD cylinders for the hot-water test (in which all cylinders entered Mode 2) was greater than that of the same cylinders in the initial experiments.

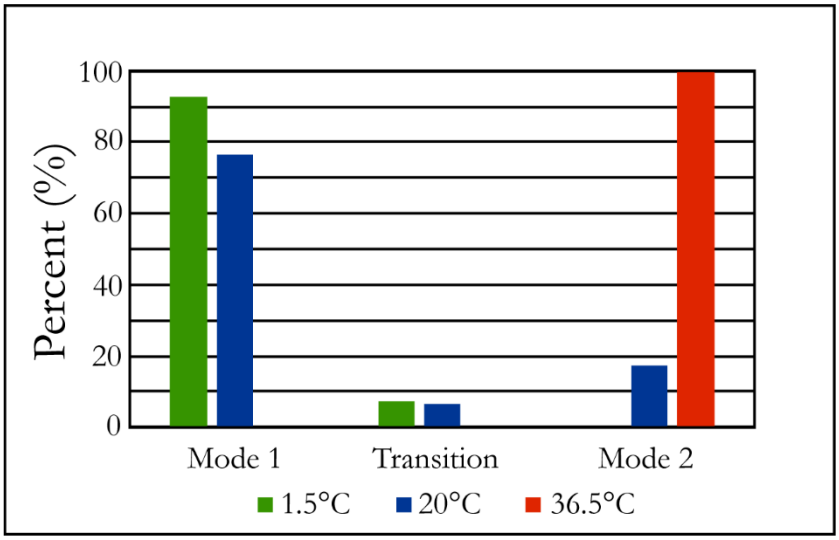

Figure 19. Percentage of $AR = 2$ CD cylinders in three modes for three different water temperatures.

Based on these results, we hypothesize that a transition regime exists for the $AR = 2$ CD cylinders beginning slightly above our targeted $Re_p = 210$. Future efforts may focus on more detailed experiments to find this threshold (see discussion in the following chapter). An overall summary of the qualitative behavior (mode) of the $AR = 2$ CD cylinders at different water temperatures is shown in Figure 19.

While the targeted Re_p in our experiments is known to be a transition threshold for the wake structure of cylinders and spheres (see discussion in Section 2.2) it is unclear how this threshold varies with cylinders of nonuniform density, or what wake instabilities might lead to the observed trajectories. However, from our data, we can make an estimate of the general range of Reynolds numbers in the transition regime for this specific class of cylinders. We plotted the average Reynolds numbers for each $AR = 2$ CD cylinder at room temperature (20˚C) based on volume-equivalent sphere diameter and average velocity magnitude, and see a noticeable difference between the mode groupings (Figure 20). The Mode 1 cylinders fall at a Reynolds number between 240 and 280, while the Mode 2 cylinders all achieve Reynolds numbers of greater than 330. The transitional cylinders lie in the range $280 < Re_p < 330$. Based on the clear separation of the two

modes, we estimate that the transition between Mode 1 and Mode may occur between $Re_p = 280$ and $Re_p = 330$. A more in-depth study of this specific cylinder class may help to narrow this range.

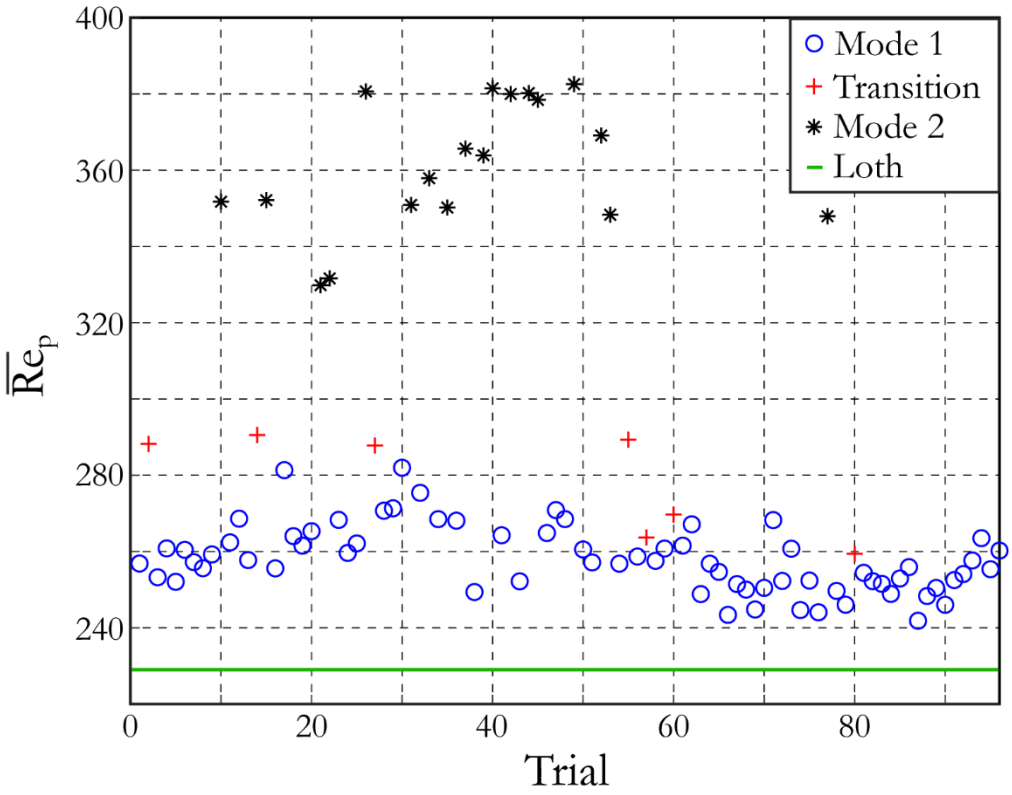

Figure 20. Average particle Reynolds number for each $AR = 2$ CD cylinder trial at room temperature ($20^{\circ}C$). The solid line is the predicted cylinder Reynolds number from [4].

It is likely that a similar transition regime exists for the $AR = 1$ CD cylinder class along with the $AR = 4$ CD cylinder class, both of which display Mode 1 or Mode 2 behavior. Since all the $AR = 1$ CD cylinders are in Mode 2, the transition threshold for this cylinder class is likely below the targeted Reynolds number of $Re_p = 210$, which was a focus for this specific study. Similarly, the transition threshold for the $AR = 4$ CD cylinders is likely to occur at higher Reynolds numbers than those tested here, since all observed cylinders in this class exhibited Mode 1 behavior. Supporting evidence of this theory can be seen in Figure 17B. The water temperature

for the $AR = 4$ CD cylinder during PIV testing was 25℃. This resulted in an orientation angle for this cylinder of around 25°, more than double the average cylinder orientation angle of an $AR = 4$ CD cylinder in previous tests (at 20℃). Future work is necessary to identify the transition threshold for these two cylinder classes.

As a final note, we caution that our use of cylinder Reynolds number to demarcate the transition between Mode 1 and Mode 2 is descriptive, and not causative. Quantitative flow visualization techniques such as PIV are necessary to uncover the mechanisms which may lead to transition, such as axisymmetry-breaking or vortex shedding in the wake. Some preliminary evidence can be seen in Figure 17, where examples of all three behavioral modes may be seen. In Mode 0 (Figure 17A; $AR = 4$ UD cylinders), the wake appears to be axisymmetric. Vortices are shed, but in a steady and regular fashion, with each vortex having a counter-rotating mirror vortex across the vertical direction. This will produce minimal oscillation in the cylinder. In Mode 1 (Figure 17B; $AR = 4$ CD cylinders), the wake is still symmetric, but is tilted due to the slanted fall velocity of the cylinder, and the leading-edge wake appears to interfere with the trailing-edge wake; this may lead to an eventual overturning of the cylinder, causing it to enter Mode 2. In Mode 2 (Figure 17C; $AR = 1$ CD cylinders), the cylinder has fully transitioned and the shed vortex wake is no longer axisymmetric; inertia and buoyant restoring torques also likely come into play as this class of cylinders oscillates around the stable “dense-end-down” vertical position. However, much more work is needed to clarify these mechanisms.

Chapter 5: Conclusions and Future Recommendations

In our experiments, we measured the landing site, orientation and terminal velocity of initially horizontal, freely falling cylinders, of both uniform density and compound density and at several aspect ratios ($1 \leq AR \leq 4$). Two high-speed cameras observed the cylinders in a 15 × 15 cm field of view, providing image data to determine cylinder velocities and trajectories. One low speed camera captured cylinder landing sites while an additional low speed camera qualitatively captured the full trajectory of each cylinder from release to impact. Additional PIV testing was performed on the three different cylinder modes discussed in Section 3.1 Cylinder landing sites, trajectories and to gain a better understanding of the wake structures present for each mode.

In the uniform density cylinders, the center of mass was co-located with the center of buoyancy; in the compound density cylinders, the center of mass was offset from the center of buoyancy. This change produced unique trajectories, orientations, and landing sites, which were categorized into three modes: Mode 0 (horizontal cylinder orientation and vertical trajectory), Mode 1 (angled cylinder orientation and angled trajectory), and Mode 2 (oscillating cylinder orientation with periodic trajectory). Mode 0 and Mode 2 behaviors were both displayed by $AR = 1$ UD cylinders. Additionally, $AR = 1$ UD cylinders showed a variation on Mode 0 in which some oscillation about the horizontal position was observed. For $AR = 1$, the CD cylinders displayed a preferred behavior in which the principal axis oscillated about a vertical position (Mode 2). This variety of behavioral modes for the $AR = 1$ cylinders may be because the range of possible projected areas for a $AR = 1$ cylinder is significantly less than the range of possible projected areas for $AR = 2$ and $AR = 4$ cylinders, which displayed more defined demarcations of behavior. In the higher AR cylinder groups, a different mode emerged (Mode 1). In this mode, cylinders fell with a stable, slanted trajectory and fixed-angle orientation. Cylinders in Mode 1 landed much farther away, on average, from the center of the tank than cylinders in Mode 2.

However, both Mode 1 and Mode 2 had an overall bias to land on the side of the landing site target where the denser end of the cylinder was initially orientated. We hypothesize that all cylinders observed to be in Mode 2 begin with a short period of time in Mode 1 before entering the measurement domain, resulting in this leftward bias.

Given the results of changing the water temperature (and therefore the kinematic viscosity), it is clear that the behavioral mode is sensitive to the cylinder Reynolds number. We hypothesize that there exists a Reynolds number threshold between 280 and 330, above which a falling compound-density cylinder will transition to Mode 2 (and below which it will remain in Mode 1). Around this threshold, we hypothesize the existence of a transition regime for the $AR = 2$ CD cylinders. These results provide a foundation on which to expand our understanding of the behavior of freely falling nonspherical particles.

Future experiments may benefit from significantly increasing the height of the experimental tank and the size of the measurement domain. Our tank height of only 61 cm is not necessarily enough to classify any of the interesting cylinder behaviors as steady state behaviors, nor can we capture all transitions; further developments in trajectory shape and character may become apparent with additional falling distance. A better knowledge of the steady state orientations of all CD cylinders would help inform our understanding of their behavior before introducing the cylinder classes into more complex flows such as turbulence. Turbulence is ubiquitous in the natural environment, where many particles of interest are found. Therefore, a future goal for this work would be to introduce the cylinders to turbulence to compare their behavior in turbulence to their behavior in quiescent flow. While we chose to start with cylinders of $AR = 1, 2 \text{ and } 4$ due to their ease of fabrication, sweeping out a wider range of AR would also be beneficial.

Lastly, the use of 3D PIV could help determine the pressure distribution around the freely-falling cylinders, providing a basis from which to calculate lift and drag forces. This would be

especially informative for the Mode 1 cylinders, as the stable slanted orientations are somewhat unique when compared to previous cylinder studies. Mode 1 cylinders at this stable slanted angle are likely to experience a nontrivial lift force, since there is a small angle of attack between the cylinder's orientation and its velocity vector. If this is truly a stable orientation, the moments generated on the cylinder by the lift, drag, gravity, and buoyancy forces must be balanced; knowledge of the acting location of lift and drag would complete the dynamic picture and help to explain the physical mechanisms maintaining the observed steady orientation. The location of lift and drag forces would also inform the development of a generalized dynamic model for non-uniform density cylinders, in which the COM location could be varied arbitrarily along the length of the cylinder. In our work, we used two COM locations (at the volumetric centroid for the UD case, and offset to one side for the CD case). However, naturally-occurring particles may have much more complex density distributions. The ability to position the COM at an arbitrary location (as would potentially be possible in a numerical/dynamic model) would be extremely helpful in predicting the physical behavior of particles of interest. In future studies, computational work in parallel with laboratory experiments may help engineers, biologists, and physicists better understand the behavior of nonspherical, non-homogeneous particles in natural environments.

References

[1] Hanratty, Thomas J.; Bandukwala, A., 1957, "Fluidization And Sedimentation Of Spherical Particles," Am. Inst. Chem. Eng., **3**(2), pp. 293–296.

[2] Fornberg, B., 1988, "Steady Viscous Flow Past A Sphere At High Reynolds Numbers," J. Fluid Mech., **190**, pp. 471–489.

[3] Delichatsios, Michael A., Probstein, R. F., 1975, "Coagulation in Turbulent Flow : Theory and Experiment," J. Colloid Interface Sci., **51**(3), pp. 394–405.

[4] Loth, E., 2008, "Drag of Non-Spherical Solid Particles of Regular and Irregular Shape," Powder Technol., **182**(3), pp. 342–353.

[5] Le Roux, J. P., 1996, "Settling Velocity Of Ellipsoidal Grains As Related To Shape Entropy," Sediment. Geol., **101**(1–2), pp. 15–20.

[6] Han, Mooyoung; Lawler, D. F., 1991, "Interactions of Two Settling Spheres: Settling Rates And Collision Efficiency," J. Hydraul. Eng., **117**(10), pp. 1269–1289.

[7] Jayaweera, K. O. L. F., and Mason, B. J., 1965, "The Behaviour of Freely Falling Cylinders and Cones in a Viscous Fluid," J. Fluid Mech., **22**(4), pp. 709–720.

[8] Reimers, P. D., and Komar, C. E., 1978, "Grain Shape Effects on Settling Rates," J. Geol., **86**(2), pp. 193–209.

[9] Komar, P. D., 2018, "Settling Velocities of Circular Cylinders at Low Reynolds Numbers," J. Geol., **88**(3), pp. 327–336.

[10] Leith, D., 1987, "Drag On Nonspherical Objects," Aerosol Sci. Technol., **6**(2), pp. 153–161.

[11] Karamanev, D. G., 1996, "Equations For Calculation Of The Terminal Velocity And Drag Coefficient Of Solid Spheres And Gas Bubbles," Chem. Eng. Commun., **147**, pp. 75–84.

[12] Mordant, N.; Pinton, J.-F., 2000, "Velocity Measurement Of A Settling Sphere," Eur.

Phys. J. B, **18**, pp. 343–352.

[13] Bagheri, G., and Bonadonna, C., 2016, “On the Drag of Freely Falling Non-Spherical Particles,” Powder Technol., **301**, pp. 526–544.

[14] Mandø, Matthias; Rosendahl, L., 2010, “On The Motion Of Non-Spherical Particles At High Reynolds Number,” Powder Technol., **202**(1), pp. 1–13.

[15] Krumbein, W. C., 1942, “Settling-velocity And Flume-behavior Of Non-spherical Particles,” Eos, Trans. Am. Geophys. Union, **23**(2), pp. 621–633.

[16] Mchenry, Matthew J; Azizi, Emanuel; Strother, J. A., 2003, “The Hydrodynamics of Locomotion at Intermediate Reynolds Numbers : Undulatory Swimming in Ascidian Larvae (Botrylloides Sp .),” J. Exp. Biol., **206**, pp. 327–343.

[17] Longmire, Ellen K.; Eaton, J. K., 1992, “Structure Of A Particle-Laden Round Jet,” J. Fluid Mech., **236**, pp. 217–257.

[18] Bocchiola, D., Catalano, F., Menduni, G., and Passoni, G., 2002, “An Analytical – Numerical Approach To The Hydraulics Of Floating Debris In River Channels,” J. Hydrol., **269**, pp. 65–78.

[19] Shanks, A. L., and Trent, J. D., 1980, “Marine Snow - Sinking Rates and Potential Role in Vertical Flux.,” Deep. Res. Part a-Oceanographic Res. Pap., **27**(2), pp. 137–143.

[20] Alldredge, A. L., and Silver, M. W., 1988, “Characteristics, Dynamics and Significance of Marine Snow,” Prog. Oceanogr., **20**(1), pp. 41–82.

[21] Beal, S. K., 2017, “Deposition Of Particles In Turbulent Flow On Channel Or Pipe Walls Channel Or Pipe Walls,” Nucl. Sci. Eng., **40**(1), pp. 1–11.

[22] Leppard, G. G., 1995, “The Characterization of Algal and Microbial Mucilages and Their Aggregates in Aquatic Ecosystems,” Sci. Total Environ., **165**(1–3), pp. 103–131.

[23] Takahashi, T., 1981, “Debris Flow,” Annu. Rev. Fluid Mech., **13**, pp. 57–77.

[24] Long, M., Moriceau, B., Gallinari, M., Lambert, C., Huvet, A., Raffray, J., and Soudant,

P., 2015, “Interactions Between Microplastics And Phytoplankton Aggregates : Impact On Their Respective Fates,” Mar. Chem., **175**, pp. 39–46.

[25] Alldredge, A. L.; Gotschalk, C. C., 1989, “Direct Observations Of The Mass Flocculation Of Diatom Blooms: Characteristics, Settling Velocities And Formation Of Diatom Aggregates,” Deep Sea Res. Part A, Oceanogr. Res. Pap., **36**(2), pp. 159–171.

[26] Asper, Vernon L.; Honjo, Susumu; Orsi, T. H., 1992, “Distribution And Transport Of Marine Snow Aggregates In The Panama Basin,” Deep Sea Res. Part A, Oceanogr. Res. Pap., **39**(6), pp. 939–952.

[27] Thomsen, L., Jamlich, S., Graf, G., Friedrichs, M., Wanner, S., and Springer, B., 1996, “An Instrument For Aggregate Studies In The Benthic Boundary Layer,” Mar. Geol., **135**, pp. 153–157.

[28] Benda, L., 1990, “The Influence of Debris Flows on Channels and Valley Floors in the Oregon Coast Range, U.S.A.,” Earth Surf. Process. Landforms, **15**, pp. 457–466.

[29] Embley, R. W., 1976, “New Evidence for Occurrence of Debris Flow Deposits in the Deep Sea,” Geology, **4**(6), pp. 371–374.

[30] Burd, Adrian B.; Jackson, G. A., 2009, “Particle Aggregation,” Ann. Rev. Mar. Sci., **1**(1), pp. 65–90.

[31] Shanks, Alan L.; Trent, J. D., 1980, “Marine Snow - Sinking Rates And Potential Role In Vertical Flux.,” Deep. Res. Part a-Oceanographic Res. Pap., **27**(2), pp. 137–143.

[32] Rau, Matthew J.; Ackleson, Steven G.; Smith, G. B., 2018, “Effects of Turbulent Aggregation OnCclay Floc Breakup and Implications for the Oceanic Environment,” PLoS One, **13**(12).

[33] Kusters, K. A. ., Wijers, J. G. ., and Thoenes, D., 1997, “Aggregation Kinetics of Small Particles in Agitated Vessels,” Chem. Eng. Sci., **52**(1), pp. 107–121.

[34] Blum, J.; Wurm, G.; Kempf, S.; Henning, T., 1996, “The Brownian Motion of Dust

Particles in the Solar Nebula : An Experimental Approach to the Problem of Pre-Planetary Dust Aggregation," Icarus, **124**(2), pp. 441–451.

[35] Soos, M., Moussa, A. S., Ehrl, L., Sefcik, J., Wu, H., and Morbidelli, M., 2008, "Effect Of Shear Rate On Aggregate Size And Morphology Investigated Under Turbulent Conditions In Stirred Tank," J. Colloid Interface Sci., **319**, pp. 577–589.

[36] Fugate, D. C., and Friedrichs, C. T., 2003, "Controls On Suspended Aggregate Size In Partially Mixed Estuaries," Estuarine, Coactal Shelf Sci., **58**, pp. 389–404.

[37] Jenny, M. ., Dusek, J. ., and Bouchet, G., 2004, "Instabilities and Transition of a Sphere Falling or Ascending Freely in a Newtonian Fluid," J. Fluid Mech., **508**, pp. 201–239.

[38] Gibbs, Ronald J.; Matthews, Martin D.; Link, D. A., 2008, "The Relationship Between Sphere Size And Settling Velocity," J. Sediment. Petrol., **41**(1), pp. 7–18.

[39] Brown, P. P., and Lawler, D. F., 2003, "Sphere Drag and Settling Velocity Revisited," J. Environ. Eng., **129**(3), pp. 222–231.

[40] le Roux, J. P., 1992, "Settling Velocity Of Spheres: A New Approach," Sediment. Geol., **81**(1–2), pp. 11–16.

[41] ten Cate, A., Nieuwstad, C. H., Derksen, J. J., and Van den Akker, H. E. A., 2002, "Particle Imaging Velocimetry Experiments And Lattice-Botlzmann Simulations On A Single Sphere Settling Under Gravity," Phys. Fluids, **14**(11), pp. 4012–4025.

[42] Chhabra, R. P.; Agarwal, L.; Sinha, N. K., 1999, "Drag on Non-Spherical Particles : An Evaluation of Available Methods," Powder Technol., **101**(3), pp. 288–295.

[43] Tran-Cong, S., Gay, M., and Michaelides, E. E., 2004, "Drag Coefficients of Irregularly Shaped Particles," Powder Technol., **139**(1), pp. 21–32.

[44] Pujara, N., Oehmke, T. B., Bordoloi, A. D., and Variano, E. A., 2018, "Rotations of Large Inertial Cubes, Cuboids, Cones, and Cylinders in Turbulence," Phys. Rev. Fluids, **3**(5), p. 054605.

[45] Kanso, E., Heisinger, L., and Newton, P., 2014, “Coins Falling in Water,” J. Fluid Mech., **742**, pp. 243–253.

[46] Zeinoddini, M., Tamimi, V., and Saeed, M., 2013, “Stream-Wise and Cross-Flow Vortex Induced Vibrations of Single Tapered Circular Cylinders : An Experimental Study,” Appl. Ocean Res., **42**, pp. 124–135.

[47] Xu, S. J. ., Zhang, W. G. ., Gan, L. ., Li, M. G. ., and Zhou, Y., 2017, “Experimental Study of Flow Around Polygonal Cylinders,” J. Fluid Mech., **812**, pp. 251–278.

[48] Marchildon, E. K.; Clamen, A.; Gauvin, W. H., 1964, “Drag And Oscillatory Motion Of Freely Falling Cylindrical Particles ’,” Can. J. Chem. Eng., **42**(4), pp. 178–182.

[49] Magarvey, R. H., and Bishop, R. L., 1961, “Transition Ranges for Three-Dimensional Wakes,” Can. J. Phys., **39**(10), pp. 1418–1422.

[50] Chung, B., Cohrs, M., Ernst, W., Galdi, G. P., and Vaidya, A., 2015, “Wake–cylinder Interactions of a Hinged Cylinder at Low and Intermediate Reynolds Numbers,” Arch. Appl. Mech., **86**(4), pp. 627–641.

[51] Yasseri, S., 2014, “Experiment of Free-Falling Cylinders in Water,” Underw. Technol., **32**(3), pp. 177–191.

[52] Abelev, A. V., Valent, P. J., and Holland, K. T., 2007, “Behavior Of A Large Cylinder In Free-Fail Through Water,” IEEE J. Ocean. Eng., **32**, pp. 10–20.

[53] Lan, J., Fleischer, P., Fan, C. W., Chu, P. C., and Gilles, A. F., 2002, “Hydrodynamics Of Falling Cylinder In Water Column,” Adv. Fluid Mech., **4**, pp. 163–181.

[54] Parsa, S., and Voth, G. A., 2014, “Inertial Range Scaling in Rotations of Long Rods in Turbulence,” Phys. Rev. Lett., **112**(2), pp. 1–5.

[55] Marcus, G. G., Parsa, S., Kramel, S., Ni, R., and Voth, G. A., 2014, “Measurements of the Solid-Body Rotation of Anisotropic Particles in 3D Turbulence,” New J. Phys., **16**.

[56] Neto, A. I. ., Demir, K., Popova, A. A. ., Oliveira, M. B. ., Mano, J. F. ., and Levkin, P. A.

., 2016, “3D Cell Culture: Fabrication of Hydrogel Particles of Defined Shapes Using Superhydrophobic-Hydrophilic Micropatterns (Adv. Mater. 35/2016),” Adv. Mater., **28**(35), p. 7552.

[57] Pedley, Derek G.; Skelly, Peter J.; Tighe, B. J., 1980, “Hydrogels In Biomedical Applications,” Br. Polym. J., **12**(3), pp. 99–110.

[58] Hoffman, A. S., 2012, “Hydrogels for Biomedical Applications ☆,” Adv. Drug Deliv. Rev., **64**, pp. 18–23.

[59] Byron, M. L., and Variano, E. A., 2013, “Refractive-Index-Matched Hydrogel Materials for Measuring Flow-Structure Interactions,” Exp. Fluids, **54**(2).

[60] Bordoloi, A. D., and Variano, E., 2017, “Rotational Kinematics of Large Cylindrical Particles in Turbulence,” J. Fluid Mech., **815**, pp. 199–222.

[61] Thielicke, W.; Stamhuis, E. J., 2014, “PIVlab - Time-Resolved Digital Particle Image Velocimetry Tool for MATLAB.”

[62] Garcia, D., 2010, “Robust Smoothing of Gridded Data in One and Higher Dimensions With Missing Values,” Comput. Stat. Data Anal., **54**(4), pp. 1167–1178.

[63] Stamhuis, E. J. ., and Videler, J. J., 1995, “Quantitative Flow Analysis Around Aquatic Animals Using Laser Sheet Particle Image Velocimetry,” J. Exp. Biol., **198**, pp. 283–294.

[64] Hedrick, T., 2019, “DLTdv Digitizing Tool.”

[65] Kwon, Y.-H., 1998, “DLT Method.”

Appendix A

Cylinder Fabrication

The same fabrication steps were completed for each cylinder batch to maintain consistency in hydrogel structure. The full list of procedural steps are listed in chronological order.

1. Fill a 2000ml beaker to 400 ml and place on hot plate to act as a hot water bath.
2. Turn on the hotplate to a temperature of 175 °F.
3. Pour 50 ml of distilled water into a beaker.
4. Pour specified amount of Agarose into this smaller beaker along with a stir bar.
5. Place this beaker with concentrated solution into the hot water bath, as shown in Figure 3A.
6. Stir solution for 25 minutes with a stir bar set to a low setting.
7. After 10 minutes, check that the solution is still around 175°F.
8. Add food coloring to the solution with 2 minutes remaining on the timer.
9. When times up, turn the stirrer up to a medium setting for a few seconds to mix the solution thoroughly and then turn the stirrer off.
10. Use the transfer/micro pipette to pour the cylinders.
11. Fill the cylinder so that the solution is exactly in line with the top surface of the mold or at the halfway point if fabricating compound density solutions.
12. Set timer to 10 minutes this time and let cylinders cool down in the aluminum mold.
13. Place the cylinders in refrigerator for an additional 3 minutes to let chill.
14. Remove cylinders from refrigerator and proceed with testing.

Appendix B

Image Calibration and Primary Variable Processing

The 22 DLT coefficients for 3D calibration were determined by mapping 48 points in global space between High Speed Camera 1 and High Speed Camera 2. Three laser-etched transparent calibration

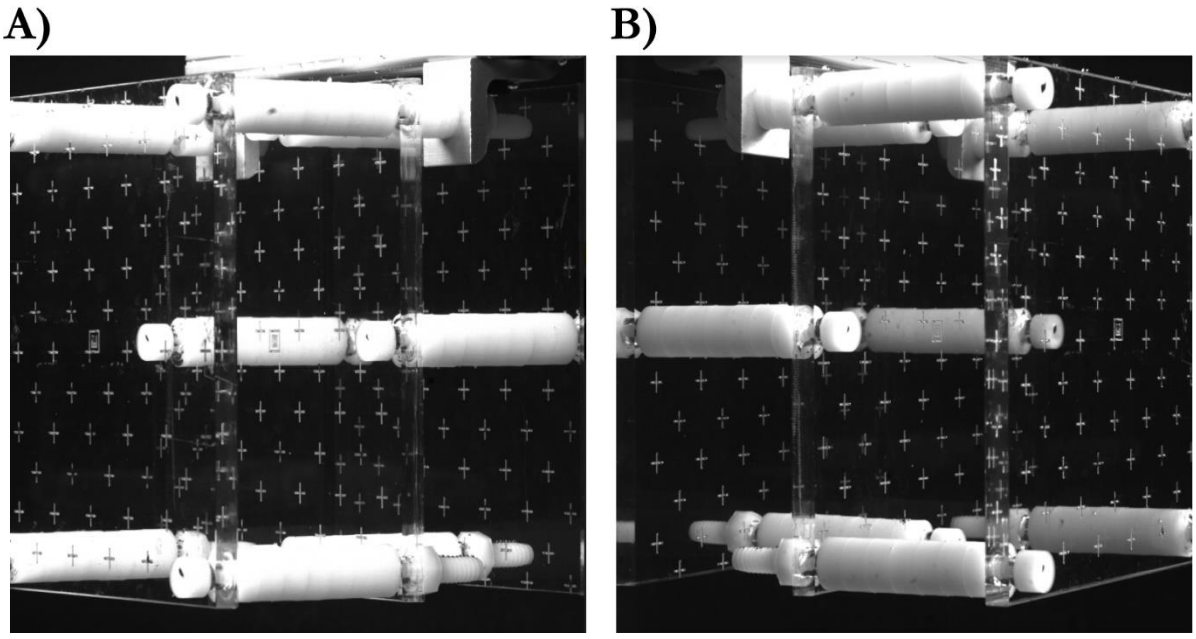

Figure 21. Images of the three evenly-spaced calibration plates as viewed from (A) High Speed Camera 1, and (B) High Speed Camera 2.

plates spaced 50 mm apart with plus signs spaced 20 mm apart were used to complete the calibration as shown in Figure 21.

Using the 22 DLT coefficients to map the 2D centroid locations from both high speed cameras into global coordinates involved matrix manipulations. Equation (16) displays a set of matrices in the form $AB = C$:

$$\begin{bmatrix} \frac{x_{c1}L_9^1 - L_1^1}{R^1} & \frac{x_{c1}L_{10}^1 - L_2^1}{R^1} & \frac{x_{c1}L_{11}^1 - L_3^1}{R^1} \\ \frac{y_{c1}L_9^1 - L_5^1}{R^1} & \frac{y_{c1}L_{10}^1 - L_6^1}{R^1} & \frac{y_{c1}L_{11}^1 - L_7^1}{R^1} \\ \frac{x_{c2}L_9^2 - L_1^2}{R^2} & \frac{x_{c2}L_{10}^2 - L_2^2}{R^2} & \frac{x_{c2}L_{11}^2 - L_3^2}{R^2} \\ \frac{y_{c2}L_9^2 - L_5^2}{R^2} & \frac{y_{c2}L_{10}^2 - L_6^2}{R^2} & \frac{y_{c2}L_{11}^2 - L_7^2}{R^2} \end{bmatrix} \begin{bmatrix} x \\ y \\ z \end{bmatrix} = \begin{bmatrix} \frac{L_4^1 - x_{c1}}{R^1} \\ \frac{L_8^1 - y_{c1}}{R^1} \\ \frac{L_4^2 - x_{c2}}{R^2} \\ \frac{L_8^2 - y_{c2}}{R^2} \end{bmatrix}, \quad (16)$$

where L^1 and L^2 values represent DLT coefficients from High Speed Camera 1 and High Speed Camera 2 respectively, and R^1 and R^2 are unknown coefficients for from High Speed Camera 1 and High Speed Camera 2 respectively; R^1 and R^2 are also functions of x, y and z. This causes the process in determining x, y and z to require iteration for solving for R^1 and R^2. Equation (17) and Equation (18) show the two equations included in the process to help solve for R^1 and R^2

$$R^1 = L_9^1\mathrm{x} + L_{10}^1\mathrm{y} + L_{11}^1\mathrm{z} + 1, \quad (17)$$

$$R^2 = L_9^2\mathrm{x} + L_{10}^2\mathrm{y} + L_{11}^2\mathrm{z} + 1, \quad (18)$$

while the parallel step to solve for x, y and z is shown in Equation (19)

$$B = (A^t \cdot A)^{-1} \cdot (A^t \cdot C), \quad (19)$$

where A^t is the transpose of matrix A. Using an initial guess for x, y and z helps begin the iterative process eventually leading to convergence.

One of the difficulties encountered with image processing occurs before any images are ever captured. Setting up the lighting is a key part in simplifying the image processing procedures. Figure 22 shows two different lighting setups used in our experiments. The setup on the left had brighter lighting allowing the cylinder to be better visualized as it fell through the high speed camera fields of view. However, the background noise and other dirt particles in the tank were also brightened making the overall image more difficult to post process. An average background image needed to be subtracted from this original image to successfully remove all noise in the final binary image.

The setup on the right showed a much darker cylinder as it fell through the high speed camera fields of view. This allowed for an easier post processing procedure. No background image subtraction was necessary to obtain a clear final binary image. We did end up subtracting a minimal background image here to stay consistent with the background subtraction technique necessary for the brighter setup.

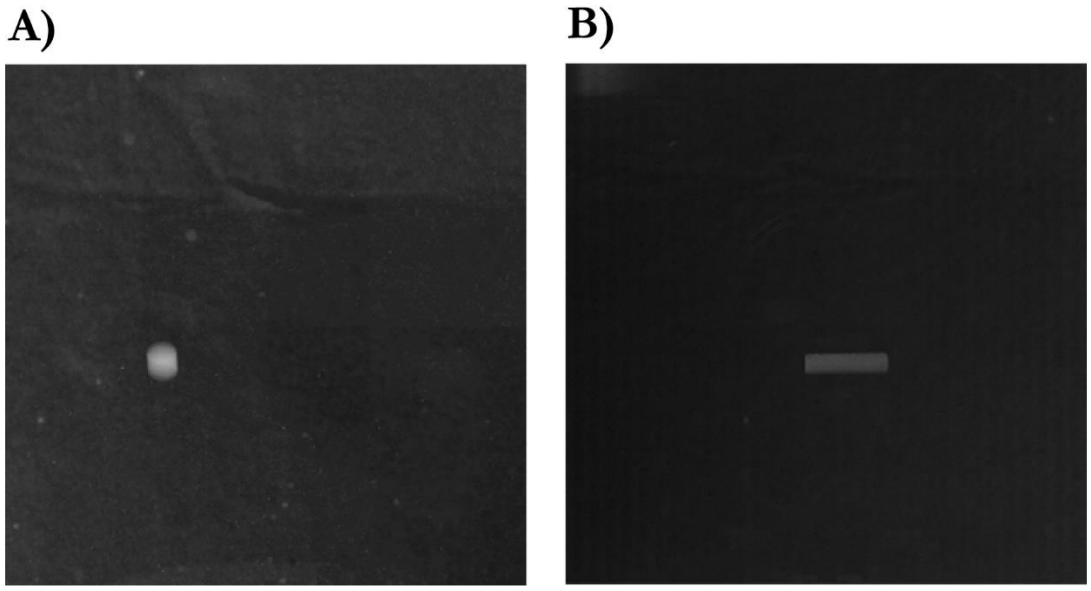

Figure 22. Background lighting (A) before improved lighting, and (B) after improved lighting.

The azimuthal angle Φ is recorded solely on the length of the bounding box of the cylinder in both high speed cameras. The coordinate system is defined so that a cylinder that is completely perpendicular to high speed camera one has an azimuthal angle equal to zero shown in Figure 23. This condition would

additionally mean the bounding rectangle length of the cylinder is equal to the actual length of the principal axis of the cylinder. As the cylinder would rotate towards or away from High Speed Camera 1, the length of the bounding rectangle would increase before decreasing at some known angle depending on cylinder dimensions. Figure 24 shows how the length of the bounding box varies as the cylinder rotates for our cylinder dimensions through Equation (14). Here, we can see that for $\mathrm{AR} = 1$, the major and minor axes of the cylinder are both 8 mm in length. As the cylinder rotates, there are always four different possible angles for one bounding box length. This is why the bounding rectangle of the cylinder from High Speed Camera 2 was necessary to determine the correct azimuthal angle of the cylinder. Furthermore, as the aspect ratio of the cylinder increased to $\mathrm{AR} = 4$, the tracking of the azimuthal angle of the cylinder through High Speed Camera 1 became extremely difficult. If a cylinder fell through the field of view of High Speed Camera 1 with an azimuthal angle between $\pm 20°$ or so, a small change in the bounding rectangle length resulted in a large change in angle measurement. First, this created a very noisy measurement of Φ over time. Additionally, if the actual length of the cylinder was 23.95 mm instead of the theoretically used value of 24 mm, a huge error would be assumed in the calculation when viewed by High Speed Camera 1. As the cylinder increases in azimuthal angle magnitude, there becomes only two options for angle selection. Since our cylinders were rarely close to perpendicular in High Speed Camera 2, we chose to use the bounding box rectangle measurements from this camera as our first processing step. While the $\mathrm{AR} = 1$ cylinders still provide four options for each case, this made the higher AR cylinder cases very manageable when determining the azimuthal angle. The bounding box length from High Speed Camera 1 was used additionally to select the overall correct value of Φ. The azimuthal angle with respect to High Speed Camera 2 was then rotated to match the defined coordinate system.

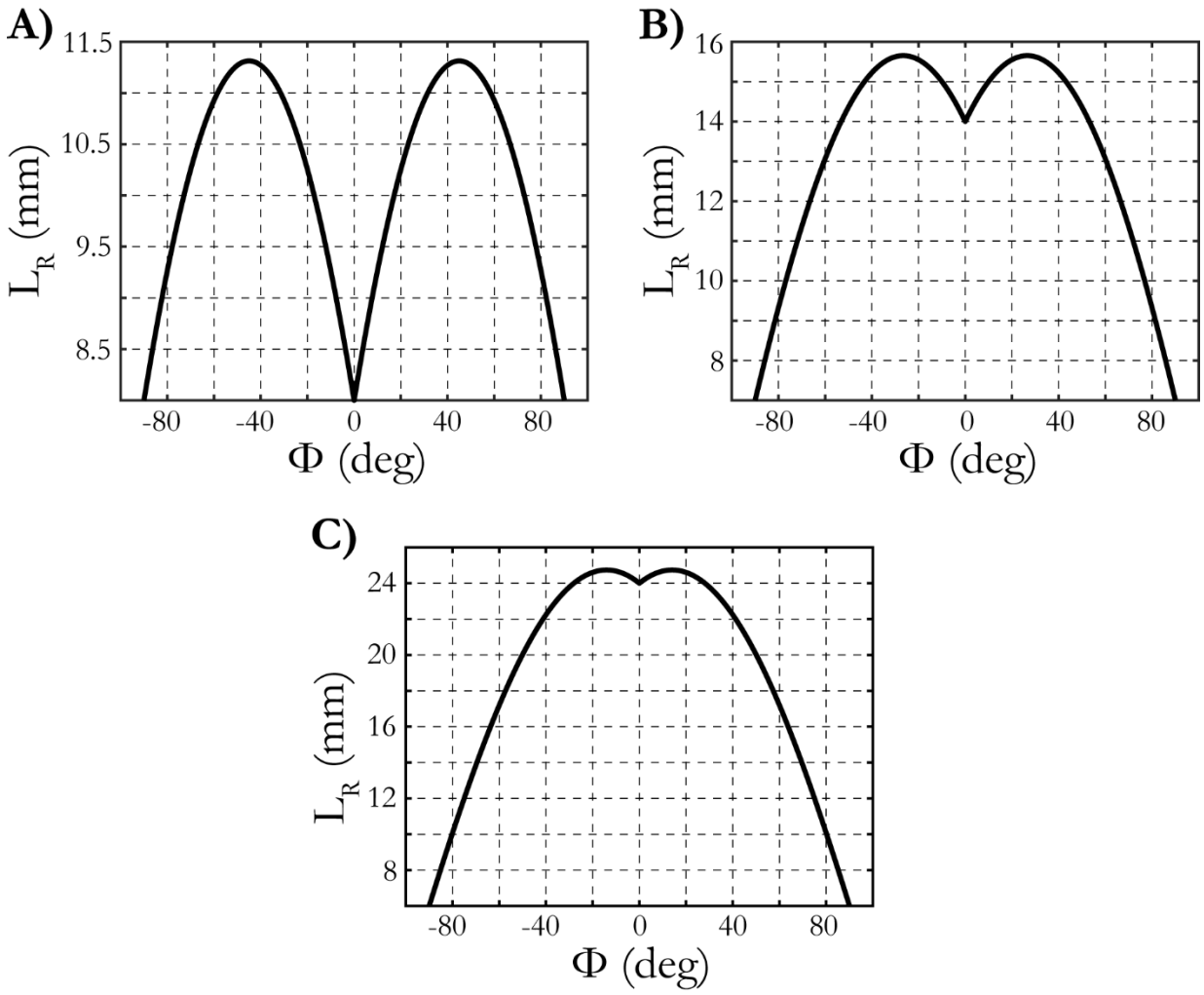

Figure 24. The different possible values of Φ for a given bounding box length for different particle dimensions, showing (A) $AR = 1$ (B) $AR = 2$, and (C) $AR = 4$.

Image Processing Code for Determining Primary Variables

This code takes in each high speed camera image and converts it into a binary image. Next, the centroid position of the cylinder, cylinder minor and major axes lengths, and cylinder major axis orientation angle is recorded for both high speed cameras in the "Drop" structure.

```
% Finding the centroid of a cylinder
clc;
clearvars -except Drop
close all

%Set image size
M=1024;
N=1024;

% first tiff number that will processed
si= 30;
% code is examining every "b" image. ex: processing every 5th image when b=5
%(Subsampling threshold)
b=1;

% Define delta t value (time between frames
dt=1/500; %[s]


%Binarizing threshold for camera 1 (higher threshold = smaller silhouette)
%(th1 can range from 0 to 1)
th1=0.01;
%Binarizing threshold for camera 2
th2=0.01;

%Connectedness structure size (for eliminating items outside ofcylinder),
%strsize1 lower bound and strsize2 upperbound.
strsize1=800; %[px]
strsize2=10000;

type={'AR1 UDP' 'AR1 CDP' 'AR2 UDP' 'AR2 CDP' 'AR4 UDP' 'AR4 CDP'}

for k=1

%Set main directory for the desired particle type
maindir=['D:\' type{k} ' 55m Lens Setup'];
%Setting  the directory where the background images are located
backdir=['D:\' type{k} ' Background Images'];
%This is the directory that has all the .tif files, in subfolders

% Lising the [mm/px] relationship for all groups in the "type" array
```

```
if k==1||k==2||k==3
  c=0.1418%[mm/px]
elseif k==5
  c=0.1408%[mm/px]
else
  c=0.1527%[mm/px]
end


%This step is necessary because the main camera was switched in PIV during
%certain cylinder groups, this is just switching those odd cases so the
%camera prefixes are all aligned during image processing
if k==4||k==5||k==6
   cam1_prefix='C002H001S';
   cam2_prefix='C001H001S';
else
   cam1_prefix='C001H001S';
   cam2_prefix='C002H001S';
end

cd(maindir)
ls_maindir=dir;
numdrops=(length(ls_maindir)-2)/2;

%Loop that iterates over all particle drop trials for a given type
for j=24:24 %numdrops
   j

    GUI_FLAG=1;
   %Set Camera 1 file directory
   dir1=[maindir '/' cam1_prefix num2str(j,'%04.f')];
   %Set Camera 2 file directory
   dir2=[maindir '/' cam2_prefix num2str(j,'%04.f')];

   cd(dir1); %Navigate to directory containing .tif files for Camera 1


   ls_1=dir;
   maxfiles=length(ls_1);
   for i=3:length(ls_1)
      temp=ls_1(i).name;
      if temp(end-3:end)=='.tif'
         fileprefix1=temp(1:end-10);
         firsttif_1=i;
         break
      end
   end

   cd(dir2)
```

```
ls_2=dir;
for i=3:length(ls_2)
   temp=ls_2(i).name;
   if temp(end-3:end)=='.tif'
      fileprefix2=temp(1:end-10);
      firstif_2=i;
      break
   end
end

n=(maxfiles-firsttif_1)-si;

%Load background images for camera 1 and camera 2
%Either a minimal or average background image was subtracted depending
%on lighting conditions
cd(backdir)
if k==4||k==5||k==6
   Z1 = imread(['avg_image_1_',num2str(j,'%04.f'), '.tif']);
   Z2 = imread(['avg_image_2_',num2str(j,'%04.f'), '.tif']);
else
   Z1 = imread(['min_image_1_',num2str(j,'%04.f'), '.tif']);
   Z2 = imread(['min_image_2_',num2str(j,'%04.f'), '.tif']);
end

for i=si:b:n %Loop through images in time

   %Pulling in images in numerical order
   cd(dir1)
   filename1=sprintf([fileprefix1 num2str(i,'%06.f') '.tif']);
   A1 = imread(filename1); %Raw Image from camera 1
   cd(dir2)
   filename2=sprintf([fileprefix2 num2str(i,'%06.f') '.tif']);
   A2 = imread(filename2); %Raw image from camera 2

   if TANKWALL==1
      %[INSERT CODE TO CROP IMAGE SO THAT FIRST X COLUMNS ARE NOT
      %VISIBLE]
      %Note: you will need to fix origin/coord system
      %A1=A1(:,165:end);
      %A2=A2(:,165:end);
   end

   % Subtracting background from camera 1 and camera 2
   A1 = A1-Z1;
   A2 = A2-Z2;

   % Binarize images using threshold as defined in first part of code
   B1 = imbinarize(A1, 'adaptive','Sensitivity',th1);
   B2 = imbinarize(A2, 'adaptive','Sensitivity',th2);

   % Removing the left 250 x columns to eliminate the side of he tank
```

```
% from field of view for the slanting cylinders
if k==4||k==6
   B1=B1(:,250:end);
else
end

% Remove any structure in B1, B2 with less than (strsize) pixels
C1 = bwareafilt(B1, [strsize1 strsize2]);
C2 = bwareafilt(B2, [strsize1 strsize2]);

% Remove connected objects on border (just in case they were missed by
% bwareaopen)
D01 = imclearborder(C1, 8);
D02 = imclearborder(C2, 8);

% Filling in any missing pieces in the Binary Image
D1 = bwconvhull(D01,'objects',4);
D2 = bwconvhull(D02,'objects',4);

% label blobs in each image(1 for main camera and 2 for side camera)
 blobs1 = bwlabel(D1,4);
 blobs2 = bwlabel(D2,4);

% Allows the user to select the correct blob in either camera if
% more than 1 blob is visable

 if max(max(blobs1))>1
    if GUI_FLAG==1
       figure
       imshow(D1)
       hold on
       [xc,yc]=ginput(1);
       yc=yc;
       xcr=round(xc);
       ycr=round(yc);
       cn1 = blobs1(ycr,xcr);
       blobs1(blobs1~=cn1)= 0;
       blobs1(blobs1>0)= 1;
       D1=blobs1;

    else

         cen1rx= round(centroid1(((i-si)/b),1));
         cen1ry= round(centroid1(((i-si)/b),2));
         cne1 = blobs1(cen1ry,cen1rx);
         blobs1(blobs1~=cne1)= 0;
         blobs1(blobs1>0)= 1;
         D1=blobs1;
    end
```

```
    else
    end

    if max(max(blobs2))>1
       if GUI_FLAG==1
          figure
          imshow(D2)
          hold on
          [xc,yc]=ginput(1);
          yc=yc;
          xcr=round(xc);
          ycr=round(yc);
          cn2 = blobs2(ycr,xcr);
          blobs2(blobs2~=cn2)= 0;
          blobs2(blobs2>0)= 1;
          D2=blobs2;

       else
            cen2rx= round(centroid2(((i-si)/b),1));
            cen2ry= round(centroid2(((i-si)/b),2));
            cne2 = blobs2(cen2ry,cen2rx);
            blobs2(blobs2~=cne2)= 0;
            blobs2(blobs2>0)= 1;
            D2=blobs2;
       end

    else

    end

%       figure(4)
%       imshow(D1)
%       figure(5)
%       imshow(D2)

    %-----------------CALCULATE DESIRED QUANTITIES-------------------------

    %Locating all x and y locations in binary image 1 where particle is
    %visable
    [r1,c1]=find(D1==1);
    %Locating all x and y locations in binary image 2 where particle is
    %visable
    [r2,c2]=find(D2==1);

    %Locating the four corners of a rectangle based on minimizing particle area
    [rectr1, rectc1, area1, perimeter1]=minboundrect(r1,c1,'a');
    [rectr2, rectc2, area2, perimeter2]=minboundrect(r2,c2,'a');

    %Creating a full matrix of points from y and x vectors
    rc1 = [rectr1 rectc1];
    rc2 = [rectr2 rectc2];
```

```
%Display image for user input to choose first tracked point
if GUI_FLAG==1
   figure
   subplot(1,2,1);
   plot(c1,1024-r1, 'bx')
   hold on
   plot(rectc1, 1024-rectr1,  'go')
   axis equal
   title('Camera 1 Column')
   hold on
   subplot(1,2,2);
   plot(c2,1024-r2, 'bx')
   hold on
   plot(rectc2, 1024-rectr2,  'go')
   axis equal
   title('Camera 2 Column')
   hold on

   %Pop up dialog box with instructions
   %f=msgbox('After closing this box, use the cursor to select the SAME primary tracking point,
first in Camera 1 and then in Camera 2. This point should be one of the two leftmost poins whose nearest
CCW neigbor makes a line along the major axis.');

   [xchoice,ychoice]=ginput(2);

   %Reset user-input y values to match existing convention for bounding box.
   ychoice=1024-ychoice;

   %Find point that is closest to the xchoice and ychoice points from the user
   %input.

   test=[rectc1-xchoice(1) rectr1-ychoice(1)];
   if isempty(test)
   break
   else
   test=(test(:,1).^2+test(:,2).^2).^0.5;
   test=test(1:4);
   check1= min(test);

   indP1=find(test==min(test));
   if numel(indP1)>1
     indP1=indP1(1,1);
   end

   indS1=mod(indP1+1,4);
   if indS1==0
     indS1=4;
   else
   end
```

```
indT1=mod(indP1+2,4);
if indT1==0
   indT1=4;
else
end


clear test
end

%Repeat for Camera 2
test=[rectc2-xchoice(2) rectr2-ychoice(2)];
if isempty(test)
   break
else
test=(test(:,1).^2+test(:,2).^2).^0.5;
test=test(1:4);
check2= min(test);

indP2=find(test==min(test));
if numel(indP2)>1
   indP2=indP2(1,1);
end

indS2=mod(indP2+1,4);
if indS2==0
   indS2=4;
else
end

indT2=mod(indP2+2,4);
if indT2==0
   indT2=4;
else
end

clear test
end

tick=1;
%IDENTIFY PRIMARY AND SECONDARY POINTS
xP1(tick)=rectc1(indP1);
xP2(tick)=rectc2(indP2);
yP1(tick)=rectr1(indP1);
yP2(tick)=rectr2(indP2);

xS1(tick)=rectc1(indS1);
xS2(tick)=rectc2(indS2);
yS1(tick)=rectr1(indS1);
yS2(tick)=rectr2(indS2);
```

```
        xT1(tick)=rectc1(indT1);
        xT2(tick)=rectc2(indT2);
        yT1(tick)=rectr1(indT1);
        yT2(tick)=rectr2(indT2);

        % angle between two selected points and horizontal
        theta1rad(tick,:) = atan2((M-yS1(tick))-(M-yP1(tick)),xS1(tick)-xP1(tick));
        theta2rad(tick,:) = atan2((M-yS2(tick))-(M-yP2(tick)),xS2(tick)-xP2(tick));

        theta1deg(tick,:) = radtodeg(theta1rad(tick));
        theta2deg(tick,:) = radtodeg(theta2rad(tick));

        %Calculate length of the major cylinder axis in pixels
        Lp1(tick,:) = sqrt((abs(xS1(tick)-xP1(tick))^2)+(abs(yS1(tick)-yP1(tick))^2));
        Lp2(tick,:) = sqrt((abs(xS2(tick)-xP2(tick))^2)+(abs(yS2(tick)-yP2(tick))^2));

        %Convert to mm
        Lp1(tick,:)=Lp1(tick)*c;
        Lp2(tick,:)=Lp2(tick)*c;

        %Same for inor cylinder axis
        Lmin1(tick,:) = sqrt((abs(xT1(tick)-xS1(tick))^2)+(abs(yT1(tick)-yS1(tick))^2));
        Lmin2(tick,:) = sqrt((abs(xT2(tick)-xS2(tick))^2)+(abs(yT2(tick)-yS2(tick))^2));

        Lmin1(tick,:)=Lmin1(tick)*c;
        Lmin2(tick,:)=Lmin2(tick)*c;

        %Calculate and store Centroid
        temp = regionprops(D1,'Centroid');
        centroid1(tick,:)=temp.Centroid; clear temp
        temp = regionprops(D2,'Centroid');
        centroid2(tick,:)=temp.Centroid;

        GUI_FLAG=0;
        tick=tick+1;
        clear xchoice ychoice
        continue
        end

    %--------------------------------------------------------------------

% %after identifying points in bounding box...
    xchoice=[xP1(tick-1) xP2(tick-1)];
    ychoice=[yP1(tick-1) yP2(tick-1)];

    %Find point that is closest to the xchoice and ychoice points from the user
    %input.
    test=[rectc1-xchoice(1) rectr1-ychoice(1)];
    if isempty(test)
        break
    else
```

```
test=(test(:,1).^2+test(:,2).^2).^0.5;
test=test(1:4);
check1= min(test);

indP1=find(test==min(test));
if numel(indP1)>1
   indP1=indP1(1,1);
end

indS1=mod(indP1+1,4);
if indS1==0
   indS1=4;
else
end

indT1=mod(indP1+2,4);
if indT1==0
   indT1=4;
else
end

clear test
end

%Repeat for Camera 2
test=[rectc2-xchoice(2) rectr2-ychoice(2)];
if isempty(test)
   break
else
test=(test(:,1).^2+test(:,2).^2).^0.5;
test=test(1:4);
check2= min(test);

indP2=find(test==min(test));
if numel(indP2)>1
   indP2=indP2(1,1);
end

indS2=mod(indP2+1,4);
if indS2==0
   indS2=4;
else
end

indT2=mod(indP2+2,4);
if indT2==0
   indT2=4;
else
end

clear test
```

```
    end

    %IDENTIFY PRIMARY AND SECONDARY POINTS
    xP1(tick)=rectc1(indP1);
    xP2(tick)=rectc2(indP2);
    yP1(tick)=rectr1(indP1);
    yP2(tick)=rectr2(indP2);

    xS1(tick)=rectc1(indS1);
    xS2(tick)=rectc2(indS2);
    yS1(tick)=rectr1(indS1);
    yS2(tick)=rectr2(indS2);

    xT1(tick)=rectc1(indT1);
    xT2(tick)=rectc2(indT2);
    yT1(tick)=rectr1(indT1);
    yT2(tick)=rectr2(indT2);

    % angle between two selected points and horizontal
    theta1rad(tick) = atan2((M-yS1(tick))-(M-yP1(tick)),xS1(tick)-xP1(tick));
    theta2rad(tick) = atan2((M-yS2(tick))-(M-yP2(tick)),xS2(tick)-xP2(tick));

    theta1deg(tick,:) = radtodeg(theta1rad(tick));
    theta2deg(tick,:) = radtodeg(theta2rad(tick));

    %Calculate the length of the major cylinder axis in pixels
    Lp1(tick,:) = sqrt((abs(xS1(tick)-xP1(tick))^2)+(abs(yS1(tick)-yP1(tick))^2));
    Lp2(tick,:) = sqrt((abs(xS2(tick)-xP2(tick))^2)+(abs(yS2(tick)-yP2(tick))^2));

    %Convert to mm
    Lp1(tick,:)=Lp1(tick)*c;
    Lp2(tick,:)=Lp2(tick)*c;

    %Same for minor axis
    Lmin1(tick,:) = sqrt((abs(xT1(tick)-xS1(tick))^2)+(abs(yT1(tick)-yS1(tick))^2));
    Lmin2(tick,:) = sqrt((abs(xT2(tick)-xS2(tick))^2)+(abs(yT2(tick)-yS2(tick))^2));

    Lmin1(tick,:)=Lmin1(tick)*c;
    Lmin2(tick,:)=Lmin2(tick)*c;

%---------------------------old calculations-------------------------

    %Calculate and store Centroid
    temp = regionprops(D1,'Centroid');
    centroid1(tick,:)=temp.Centroid; clear temp
    temp = regionprops(D2,'Centroid');
    centroid2(tick,:)=temp.Centroid;

    tick=tick+1;
  end
```

```
    %Change origin so that origin is at bottom left (not top left)
    centroid1(:,2)=1024-centroid1(:,2);
    centroid2(:,2)=1024-centroid2(:,2);
  %Store all properties of interest in the variable Drop
    Drop(j).theta1deg=theta1deg;
    Drop(j).theta2deg=theta2deg;
    Drop(j).Lp1=Lp1;
    Drop(j).Lp2=Lp2;
    Drop(j).Lmin1=Lmin1;
    Drop(j).Lmin2=Lmin2;
    Drop(j).centroid1=centroid1;
    Drop(j).centroid2=centroid2;
    Drop(j).tick=tick-1;

    clear theta* centroid* Lp1 Lp2 Lmin1 Lmin2

    cd('D:\RESULTS_Feb2019')
    save(type{k},'Drop')

end
end
```

Appendix C

Secondary Variable Processing Codes

Code to calculate 3D centroid locations

15. This code uses the iterative process discussed in Appendix B to determine the global location of each cylinder's centroid location. A rotation of the coordinate system is also performed to align the global system with the coordinate system defined in this Thesis. This code spits out a 3D plot of the trajectories, a $x-z$ view plot, a $x-y$ view plot, and an orientation plot of the cylinders principal axis.

```
%-------------STEP ONE: LOAD CONSTANTS AND KEY VBLS-----------------------

clc
close all
clear all

%number of rows in Drop structure

%All types of variables being evaluated
type={'AR1 UDP' 'AR1 CDP' 'AR2 UDP' 'AR2 CDP' 'AR4 UDP' 'AR4 CDP'};

for k=4
   maindir=['D:\Drop Structures For Thesis'];
   cd(maindir)
   load(type{k})

   %inputting number of drops for each cylinder group
   if k==2||k==3||k==5
      nDrops = 100;
   elseif k==1
      nDrops = 97;
   elseif k==6
      nDrops = 93;
   else
      nDrops = 96
   end


   if k==1||k==2||k==3
      theta=61.65
```

```
    elseif k==4||k==6
        theta=60.10
    else
        theta=57.44
    end

    % This reads "11" DLT coefficients into matlab for both cameras
% L camera is the main camera and R camera is the camera at 120 degrees

if k==1||k==2||k==3
   load DLT_Setup1.mat
elseif k==5
   load DLT_Setup2.mat
else
   load DLT_Setup3.mat
end

%Loading in the camera one(L1-L11) and camera 2 (S1-S11) DLT coefficients
%from a saved mat file
L1=DLTmat(1,1);
L2=DLTmat(2,1);
L3=DLTmat(3,1);
L4=DLTmat(4,1);
L5=DLTmat(5,1);
L6=DLTmat(6,1);
L7=DLTmat(7,1);
L8=DLTmat(8,1);
L9=DLTmat(9,1);
L10=DLTmat(10,1);
L11=DLTmat(11,1);
S1=DLTmat(1,2);
S2=DLTmat(2,2);
S3=DLTmat(3,2);
S4=DLTmat(4,2);
S5=DLTmat(5,2);
S6=DLTmat(6,2);
S7=DLTmat(7,2);
S8=DLTmat(8,2);
S9=DLTmat(9,2);
S10=DLTmat(10,2);
S11=DLTmat(11,2);

% j refers to the Drop being processed
for j=1:nDrops
    tick=1;

% i refers to the numbers of images in Drop(j)
for i=1:Drop(j).tick
```

```
%We are ignoring optical errors in this matrix so delta u and delta v in
%from kwon3D website in equation(matrix 22) are equal to zero, therefore
%our u and v are equal to swirly v and w respectively

%Guess an x,y, and z to start iterative process, accounting for tank in FOV
%for two particle groups
if k==4||k==6
p1x=Drop(j).centroid1(i,1)+(250);
p1y=Drop(j).centroid1(i,2);
p2x=Drop(j).centroid2(i,1);
p2y=Drop(j).centroid2(i,2);
else
p1x=Drop(j).centroid1(i,1);
p1y=Drop(j).centroid1(i,2);
p2x=Drop(j).centroid2(i,1);
p2y=Drop(j).centroid2(i,2);
end

x = 0.1;
y = 0.1;
z = 0.1;

%labeling these variables with a random guess to be recalculated later
pex = 10;
pey = 10;
pez = 10;

%Setting the previous iteration threshold
while pex >= 0.001 && pey >= 0.001 && pez >= 0.001

%Solves for an R1 and R2 value for each iteration
R1=(L9*x)+(L10*y)+(L11*z)+1;
R2=(S9*x)+(S10*y)+(S11*z)+1;

%matrix calculations from kwon 3D
A=[((p1x*L9)-L1)/R1 ((p1x*L10)-L2)/R1 ((p1x*L11)-L3)/R1; ((p1y*L9)-L5)/R1 ((p1y*L10)-L6)/R1
((p1y*L11)-L7)/R1;...
   ((p2x*S9)-S1)/R2 ((p2x*S10)-S2)/R2 ((p2x*S11)-S3)/R2; ((p2y*S9)-S5)/R2 ((p2y*S10)-S6)/R2
((p2y*S11)-S7)/R2];

B=[(L4-p1x)/R1; (L8-p1y)/R1; (S4-p2x)/R2; (S8-p2y)/R2];


%matrix maniuplation from kwon 3D
vbl=(inv((transpose(A)*A)))*(transpose(A)*B);

xn=vbl(1,1);
yn=vbl(2,1);
zn=vbl(3,1);

pex= (xn-x)/x;
```

```
pey= (yn-y)/y;
pez= (zn-z)/z;


x=xn;
y=yn;
z=zn;

%rotating the coordinate system by roughly 60 degrees to match the desired
%coordinate sytem with respect to camera 1. The AR2 CDP and AR4 CDP were
%also translated 7 cm.
if k==4||k==6
   xrot= ((xn*cosd(theta))-(zn*sind(theta)))-.07;
else
   xrot= (xn*cosd(theta))-(zn*sind(theta));
end
yrot= yn;
zrot= (xn*sind(theta))+(zn*cosd(theta));

tick=i;

end

Cord(i,:)=[xrot yrot zrot];


end
Position(j).Cord=(Cord*100);
Position(j).Ptick=tick;

Drop(j).Cord=(Cord*100);
Drop(j).tickcheck=tick;

clear Cord

end

save(type{k},'Drop')

end
%%

figure(1)
for j=1:nDrops;
   plot3(Drop(j).Cord(:,1),Drop(j).Cord(:,2),Drop(j).Cord(:,3));
   hold on
   xlabel('x position (cm)')
   ylabel('y position (cm)')
   zlabel('z position (cm)')
      if k==4||k==6
      axis([-17 3 -10 10 -10 10]);
```

```
        else
        axis([-10 10 -10 10 -10 10]);
    end

end

%%
hold off

figure(2)
% subplot(2,1,1)
linecolors=winter(nDrops);
for j=1:nDrops
    plot(Drop(j).Cord(:,1),Drop(j).Cord(:,2), 'color',linecolors(j,:));
    if k==4||k==6
        axis([-13 -1 -6 6]);
    else
        axis([-6 6 -6 6])
    end
    hold on
    %title('AR1 UDP Centroid Tracking')
    grid on
    set(gca, 'Fontsize', 13, 'Linewidth', 0.75, 'fontname', 'Tw Cen MT')
    xlabel('x (cm)','FontSize', 18, 'fontname', 'Tw Cen MT')
    ylabel('y (cm)','FontSize', 18, 'fontname', 'Tw Cen MT')

end

figure(3)
linecolors=winter(nDrops);
for j=1:nDrops;
    plot(Drop(j).Cord(:,1),Drop(j).Cord(:,3), 'color',linecolors(j,:));
    if k==4||k==6
        axis([-13 -1 -6 6]);
    else
        axis([-6 6 -6 6])
    end
    hold on
    grid on
    %title('AR1 UDP Centroid Tracking')
    set(gca, 'Fontsize', 13, 'Linewidth', 0.75, 'fontname', 'Tw Cen MT')
    xlabel('x (cm)','FontSize', 18, 'fontname', 'Tw Cen MT')
    ylabel('z (cm)','FontSize', 18, 'fontname', 'Tw Cen MT')

end

figure(4)
linecolors=winter(nDrops);
for j=1:nDrops;

    if k==2
```

```
    theta=Drop(j).theta1deg+180;
    elseif k==1
    thetamin=(Drop(j).theta1deg(1));
       if thetamin<-50
          theta=Drop(j).theta1deg+180;
       else
          theta=Drop(j).theta1deg;
       end
    elseif k==4
           thetamin=(Drop(j).theta1deg(1));
       if thetamin<-50
          theta=Drop(j).theta1deg+180;
       else
          theta=Drop(j).theta1deg;
       end
    else
    theta=Drop(j).theta1deg;
    end

    thetasmooth = smoothdata(theta,'sgolay');

    plot(thetasmooth,Drop(j).Cord(:,2), 'color',linecolors(j,:));

    axis([-180 180 -6 6]);

    hold on
    grid on
    %title('AR1 UDP \theta Orientation')
    set(gca, 'Fontsize', 13, 'Linewidth', 0.75, 'fontname', 'Tw Cen MT')
    xlabel(' \theta (deg)','FontSize', 18, 'fontname', 'Tw Cen MT')
    ylabel('y (cm)','FontSize', 18, 'fontname', 'Tw Cen MT')

    clear theta thetasmooth

end
```

Code to calculate Φ for each trial

This code takes in the major and minor axes cylinder lengths as well as the orientation angle from both high speed cameras. It spits out the orientation of each cylinder of time for all trials in a cylinder class. The Φ values are recorded and saved in the "Drop" structure.

```
%-------------STEP ONE: LOAD CONSTANTS AND KEY VBLS-----------------------

clc
close all
clearvars -except Drop DropPhi

%number of rows in Drop structure
nDrops = 100;

%All types of variables being evaluated
type={'AR1 UDP' 'AR1 CDP' 'AR2 UDP' 'AR2 CDP' 'AR4 UDP' 'AR4 CDP'};

for k=2
   maindir=['D:\Drop Structures For Thesis'];
   cd(maindir)
   load(type{k})

   %Paritcle dimensions used in calculations allowing for shrinkage
   if k==1||k==2
      Dp=7.7;
      La=7.7;
   elseif k==3||k==4
      Dp=7.0;
      La=13.5;
   else
      Dp=6.0;
      La=23.0;
   end

phi(:,1)=-90:0.01:90;

for i=1:numel(phi)
Lbb(i,1)=La*cosd(phi(i))+Dp*abs(sind(phi(i)));
phimat(i,1)=Lbb(i,1);
phimat(i,2)=phi(i,1);
end

% j refers to the Drop being processed
for j=1:100       %:nDrops
j
imnum=1;
% i refers to the numbers of images in Drop(j)
for i=1:Drop(j).tick
```

```
%Pull in the major axis lengths of the cylinder from both camera views
Lp1=Drop(j).Lp1(i);
Lp2=Drop(j).Lp2(i);


if k==1 || k==2

   if Lp1<Dp
      Lp1=Dp;
   else
   end

   if Lp2<Dp
      Lp2=Dp;
   else
   end
else
end

if Lp1>=max(phimat(:,1))
   Lp1=max(phimat(:,1));
end

if Lp2>=max(phimat(:,1))
   Lp2=max(phimat(:,1));
end

psi= asind(La/(sqrt((La^2)+(Dp^2))));
alpha1= asind(Lp1/(sqrt((La^2)+(Dp^2))));
phi1c= alpha1-psi;

if phi1c>=0
   phi1(1)=phi1c;
   phi1(2)=-1*phi1c;
   phi1(3)=180-alpha1-psi;
   phi1(4)=-1*phi1(3);
end

if phi1c<0
   phi1(1)=180-alpha1-psi;
   phi1(2)=-1*phi1(1);
end
 %%Unlock this if particle fails under first attempt
%  if imnum==1
%     if Lp2>Lp1
%        phif=max(phi1)
%        Angle(i,:)=phif;
%        imnum=imnum+1
%        continue
%     else
```

```
%        phif=phi1(2)
%        Angle(i,:)=phif;
%        imnum=imnum+1
%        continue
%     end
% end

%%Lock this feature for the particles that fail during initial trial
 phi1(phi1<-35 | phi1>35) = [];

ec=isempty(phi1);
if ec==1
   phif=Angle(i-1);
   Angle(i,:)=phif;
   continue
else
end

alpha2= asind(Lp2/(sqrt((La^2)+(Dp^2))));
phi2c= alpha2-psi;

if phi2c>=0
    phi2(1)=phi2c;
    phi2(2)=-1*phi2c;
    phi2(3)=180-alpha2-psi;
    phi2(4)=-1*phi2(3);

    for s=1:numel(phi2)
        if phi2(s)<=30
            phi2(s)= phi2(s)+60;
        else
            phi2(s)= phi2(s)-120;
        end
    end
end

if phi2c<0
    phi2(1)=180-alpha2-psi;
    phi2(2)=-1*phi2(1);

    for s=1:numel(phi2)
        if phi2(s)<=30
            phi2(s)= phi2(s)+60;
        else
            phi2(s)= phi2(s)-120;
        end
    end
end

if imnum==1
```

```
for v=1:length(phi1)
  for u=1:length(phi2)
     difmat(v,u)=abs(phi1(v)-phi2(u));

  end
end

[var1,var2]=find(difmat==min(min(difmat)));

phif= (phi1(var1)+phi2(var2))/2;

if length(phif)>=2

   phif=phif(1,1);

else
end

else
 matcheck1=repmat(Angle(i-1),[1 length(phi1)]);
 matcheck2=repmat(Angle(i-1),[1 length(phi2)]);

 [minValue1,closestIndex1] = min(abs(matcheck1-phi1));
 [minValue2,closestIndex2] = min(abs(matcheck2-phi2));

phif = phi2(closestIndex2);
end

imnum=imnum+1;

Angle(i,:)=phif;
tick(i,:)=i;

clear phi1 phi2 phif difmat matcheck1 matcheck2 minValue1 minValue2 closestIndex1 closestIndex2

end

DropPhi(j).phiw=Angle
Drop(j).phiw=Angle;

clear Angle

save(type{k},'Drop')

end
end
```

Appendix D

Data Analysis Codes

T-testing variable generation code

This code takes in data from a specific cylinder class and saves all the average values and standard deviations of the parameters evaluated during the t-testing in this Thesis. These values are stored in the "Drop" structure.

```
%-------------STEP ONE: LOAD DROP STRUCTURES -----------------------

clc
close all
clear all

%b is refering to the image subsample number (here we are looking at every
%10th image to allow the centroid to travel at least two pixels in every particle group)
b=10;
%calculating delta t based on frame rate and "b"
dt=(1/500)*b;

type={'AR1 UDP' 'AR1 CDP' 'AR2 UDP' 'AR2 CDP' 'AR4 UDP' 'AR4 CDP'};

for f=6
   maindir=['D:\Drop Structures For Thesis'];
   cd(maindir)
   load(type{f})

     tick=1;
   for j=1:numel(Drop)

      x=Drop(j).Cord(:,1);
      y=Drop(j).Cord(:,2);
      z=Drop(j).Cord(:,3);
      theta=Drop(j).theta1deg;
      phiw=Drop(j).phiw;

      n=1;
      for i=1:b:numel(x)
         xss(n,:)=x(i);
         yss(n,:)=y(i);
         zss(n,:)=z(i);

         n=n+1;
      end
```

```
    xss = smoothdata(xss,'sgolay',50);
    yss = smoothdata(yss,'sgolay',50);
    zss = smoothdata(zss,'sgolay',50);
    theta = smoothdata(theta,'sgolay',50);
    phiw = smoothdata(phiw,'sgolay',50);

    xrange = abs((max(xss))-(min(xss)));
    yrange = abs((max(yss))-(min(yss)));
    zrange = abs((max(zss))-(min(zss)));

    for u=2:numel(xss)
        xvel(u-1)=(xss(u)-xss(u-1))/dt;
        yvel(u-1)=(yss(u)-yss(u-1))/dt;
        zvel(u-1)=(zss(u)-zss(u-1))/dt;

    end

        xvelavg=mean(xvel);
        yvelavg=mean(yvel);
        zvelavg=mean(zvel);
        thetaavg=mean(theta);
        thetavar=var(theta);
        phiwvar=var(phiw);
        uvar=var(xvel);
        vvar=var(yvel);
        wvar=var(zvel);

    vmat(tick,1)= xvelavg ;
    vmat(tick,2)= yvelavg ;
    vmat(tick,3)= zvelavg ;
    thetamat(tick,1)= thetaavg ;
    rangemat(tick,1)= xrange ;
    rangemat(tick,2)= yrange ;
    rangemat(tick,3)= zrange ;
    varmat(tick,1)= thetavar ;
    uvarmat(tick,1)=uvar;
    vvarmat(tick,1)=vvar;
    wvarmat(tick,1)=wvar;
    phiwvarmat(tick,1)=phiwvar;

    tick=tick+1;

    clearvars -except Drop vmat b dt f j tick type thetamat rangemat varmat uvarmat vvarmat wvarmat
phiwvarmat

    end
    axv=mean(vmat(:,1));
    sdxv=std(vmat(:,1));
    ayv=mean(vmat(:,2));
    sdyv=std(vmat(:,2));
```

```
azv=mean(vmat(:,3));
sdzv=std(vmat(:,3));

atheta=mean(thetamat(:,1));
sdtheta=std(thetamat(:,1));

athetavar=mean(varmat(:,1));
sdthetavar=std(varmat(:,1));

axrange=(mean(rangemat(:,1)));
sdxrange=(std(rangemat(:,1)));
ayrange=(mean(rangemat(:,2)));
sdyrange=(std(rangemat(:,2)));
azrange=(mean(rangemat(:,3)));
sdzrange=(std(rangemat(:,3)));

auvar=mean(uvarmat(:,1));
sduvar=std(uvarmat(:,1));
avvar=mean(vvarmat(:,1));
sdvvar=std(vvarmat(:,1));
awvar=mean(wvarmat(:,1));
sdwvar=std(wvarmat(:,1));

aphiwvar=mean(phiwvarmat(:,1));
sdphiwvar=std(phiwvarmat(:,1));

Drop(1).axv=axv
Drop(1).sdxv=sdxv
Drop(1).ayv=ayv
Drop(1).sdyv=sdyv
Drop(1).azv=azv
Drop(1).sdzv=sdzv

Drop(1).atheta=atheta
Drop(1).sdtheta=sdtheta

Drop(1).athetavar=athetavar
Drop(1).sdthetavar=sdthetavar

Drop(1).axrange=axrange
Drop(1).sdxrange=sdxrange
Drop(1).ayrange=ayrange
Drop(1).sdyrange=sdyrange
Drop(1).azrange=azrange
Drop(1).sdzrange=sdzrange

Drop(1).auvar=auvar
Drop(1).sduvar=sduvar
Drop(1).avvar=avvar
Drop(1).sdvvar=sdvvar
Drop(1).awvar=awvar
```

```
    Drop(1).sdwvar=sdwvar

    Drop(1).aphiwvar=aphiwvar
    Drop(1).sdphiwvar=sdphiwvar

   maindir=['D:\Drop Structures For Thesis'];
   cd(maindir)
   save(type{f},'Drop')
end
```

Upaired t-test results code

This code is used to determine the t-value for similar aspect ratio classes. The user must change the parameter being tested between tests. The t-values were then documented in an excel spreadsheet for later comparison.

```
%-------------STEP ONE: LOAD DROP STRUCTURES ------------------------

clc
close all
clear all

type={'AR1 UDP' 'AR1 CDP' 'AR2 UDP' 'AR2 CDP' 'AR4 UDP' 'AR4 CDP'};

    f=3;
    maindir=['D:\Drop Structures For Thesis'];
    cd(maindir)
    load(type{f})

    n1=numel(Drop);
    x1bar=Drop(1).axv;
    s1=Drop(1).sdxv;

    clear Drop

    f=5;
    maindir=['D:\Drop Structures For Thesis'];
    cd(maindir)
    load(type{f})

    n2=numel(Drop);
    x2bar=Drop(1).axv;
    s2=Drop(1).sdxv;

    a=abs(x1bar-x2bar);
    b=((n1-1)*(s1^2))+((n2-1)*(s2^2));
    c=(n1-1)+(n2-1);
    d=(1/n1)+(1/n2);

    t= a/(sqrt((b/c)*d));
```

PIV vorticity analysis code

This code as an example of one of the vorticity plots shown in this Thesis. The vorticity values calculated for a certain image in PIVlab are read into Matlab and plotted over a certain section of the field of view. The plotted section changes for each image based upon cylinder location.

```
clear all
close all
clc

load('AR4CDP_Image64_FILT0.3.mat')
U=u_filtered;
V=v_filtered;

clearvars -except U V vorticity
[cal_mat,grid_y,grid_x]=vortex_computation(U ,V,'Lamda','sec_order',0.0001548,1,12)
[vortex_centers,circulation]=vortex_identification(cal_mat,5000,1,U,V,0.0001548,12)

% figure(2);
% pcolor(vorticity); shading flat
% hold on
% scatter(vortex_centers(:,1),vortex_centers(:,2),'filled','k');
% set(gca,'Ydir','reverse')
% axis equal

vorticity = vorticity*50

figure(3);
contourf(vorticity(:,16:50));
contourcmap('jet');
hold on
maindir=['D:\PIV Test Videos 030519\C001H001S0007'];
cd(maindir)
set(gca,'Ydir','reverse')
A1= imread('AR4CDP_mask7_0064.tif');
A1= A1(12:12:end-12,12:12:end-12);
B1=A1(:,16:50);
[r c]=find(B1==1);
plot(c,r,'mx')

axis equal
```

Appendix E

Discussion Particle Codes

Separating AR2 CD cylinders into three groups code

This code splits the cylinder trials for the $AR = 2$ CD cylinder class into two different groups based on maximum orientation angle. The transitional cylinders are also included in this code's calculations. The velocities for each cylinder trial are plotted over time within each cylinder group. This code also calculates the average Reynolds for each cylinder trial and spits out the plot used in the Discussion section.

```
clc
close all
clearvars -except Drop


type={'AR1 UDP' 'AR1 CDP' 'AR2 UDP' 'AR2 CDP' 'AR4 UDP' 'AR4 CDP'};

%evaluating every "h" image during processing
h=10;
%calculating delta t based on frame rate and "h"
dt=(1/500)*h;

%setting the upper and lower cuttoff angles when separting cylinders into
%groups
upcutang=75;
lowcutang=35;

for f=4
   maindir=['D:\Drop Structures For Thesis'];
   cd(maindir)
   load(type{f})

   tick1=1;
   tick2=1;



   for p=1:96
      theta=Drop(p).theta1deg;


      a=abs(max(theta));
```

```
        b=abs(min(theta));

        if b>a
           a=b;
        else
        end


        if a>upcutang || b>upcutang
           anglesep(p,:)=1;

        elseif a>lowcutang & a<upcutang
           anglesep(p,:)=2;

        else
           anglesep(p,:)=0;
        end

        clear theta a b
    end

 linecolors=winter(96);
for j=1:96

    L=14.0;
    D=7.0;
    Deq=10.1;

    mu1=0.0000009795

x=Drop(j).Cord(:,1);
y=Drop(j).Cord(:,2);
z=Drop(j).Cord(:,3);

theta=Drop(j).theta1deg;
phiw=Drop(j).phiw;


nn=1
for i=1:h:numel(x)
xss(nn,:)=x(i);
yss(nn,:)=y(i);
zss(nn,:)=z(i);

nn=nn+1;
end

 xss = smoothdata(xss,'sgolay',50);
 yss = smoothdata(yss,'sgolay',50);
 zss = smoothdata(zss,'sgolay',50);
```

```
for u=2:numel(xss)
   xvel(u-1)=(xss(u)-xss(u-1))/dt;
   yvel(u-1)=(yss(u)-yss(u-1))/dt;
   zvel(u-1)=(zss(u)-zss(u-1))/dt;

end

uavg(j,1)=mean(xvel);
vavg(j,1)=mean(yvel);
wavg(j,1)=mean(zvel);

vmag(j,1)=sqrt(((uavg(j,1))^2)+((vavg(j,1))^2)+((wavg(j,1))^2));

ReDeq(j,1)= (((vmag(j,1))/100)*(Deq/1000))/mu1;


xrange = abs((max(xss))-(min(xss)));
yrange = abs((max(yss))-(min(yss)));
zrange = abs((max(zss))-(min(zss)));

xvelavg=mean(xvel);
yvelavg=mean(yvel);
zvelavg=mean(zvel);
thetaavg=mean(theta);
thetavar=var(theta);
phiwvar=var(phiw);
uvar=var(xvel);
vvar=var(yvel);
wvar=var(zvel);

for e=1:numel(yvel)
   t(e)=(e-1)*dt ;
end

if anglesep(j,:)==1

   vmat1(tick1,1)= xvelavg ;
   vmat1(tick1,2)= yvelavg ;
   vmat1(tick1,3)= zvelavg ;
   thetamat1(tick1,1)= thetaavg ;
   rangemat1(tick1,1)= xrange ;
   rangemat1(tick1,2)= yrange ;
   rangemat1(tick1,3)= zrange ;
   varmat1(tick1,1)= thetavar ;
   uvarmat1(tick1,1)=uvar;
   vvarmat1(tick1,1)=vvar;
   wvarmat1(tick1,1)=wvar;
   phiwvarmat1(tick1,1)=phiwvar;

   tick1=tick1+1
```

```
    figure(10)
    plot(t,yvel, 'color',linecolors(j,:))
    hold on
    set(gca, 'Fontsize', 13, 'Linewidth', 0.75, 'fontname', 'Tw Cen MT')
    xlabel('time (s)','FontSize', 18, 'fontname', 'Tw Cen MT')
    ylabel('v (cm/s)','FontSize', 18, 'fontname', 'Tw Cen MT')
    grid on
    axis([0 6 -4 -2])

    figure(3)
    scatter(j,ReDeq(j,1),'*','r')
    hold on
    xlabel('Drop #')
    ylabel('ReDeq')
    axis([0 96 220 400])
    grid on
    legend('ReDeq','Re Loth at 20^oC')

    print('AR2CDPS','-dpng','-r300')

elseif anglesep(j,:)==2
    figure(30)
    plot(t,yvel, 'color',linecolors(j,:))
    hold on
    set(gca, 'Fontsize', 13, 'Linewidth', 0.75, 'fontname', 'Tw Cen MT')
    xlabel('time (s)','FontSize', 18, 'fontname', 'Tw Cen MT')
    ylabel('v (cm/s)','FontSize', 18, 'fontname', 'Tw Cen MT')
    grid on
    axis([0 6 -4 -2])

    figure(3)
    scatter(j,ReDeq(j,1),'+','b')
    hold on
    xlabel('Drop #')
    ylabel('ReDeq')
    axis([0 96 220 400])
    grid on
    legend('ReDeq','Re Loth at 20^oC')

    print('AR2CDPT','-dpng','-r300')

else

    vmat2(tick2,1)= xvelavg ;
    vmat2(tick2,2)= yvelavg ;
    vmat2(tick2,3)= zvelavg ;
    thetamat2(tick2,1)= thetaavg ;
    rangemat2(tick2,1)= xrange ;
    rangemat2(tick2,2)= yrange ;
    rangemat2(tick2,3)= zrange ;
```

```
    varmat2(tick2,1)= thetavar ;
    uvarmat2(tick2,1)=uvar;
    vvarmat2(tick2,1)=vvar;
    wvarmat2(tick2,1)=wvar;
    phiwvarmat2(tick2,1)=phiwvar;

    tick2=tick2+1

    figure(20)
    plot(t,yvel, 'color',linecolors(j,:))
    hold on
    set(gca, 'Fontsize', 13, 'Linewidth', 0.75, 'fontname', 'Tw Cen MT')
    xlabel('time (s)','FontSize', 18, 'fontname', 'Tw Cen MT')
    ylabel('v (cm/s)','FontSize', 18, 'fontname', 'Tw Cen MT')
    grid on
    axis([0 6 -4 -2])
    print('AR2CDPTRAN','-dpng','-r300')

    figure(3)
    scatter(j,ReDeq(j,1),'o','g')
    hold on
    xlabel('Drop #')
    ylabel('ReDeq')
    axis([0 96 220 400])
    grid on
    legend('ReDeq','Re Loth at 20^oC')
end

%clear xvel yvel zvel xss yss zss x y z t

clearvars -except Drop h dt f j tick1 tick2 type vmat1 thetamat1 rangemat1 varmat1 uvarmat1 vvarmat1
wvarmat1 phiwvarmat1 vmat2 thetamat2 rangemat2 varmat2 uvarmat2 vvarmat2 wvarmat2 phiwvarmat2
anglesep linecolors
end

end

    axv1=mean(vmat1(:,1));
    sdxv1=std(vmat1(:,1));
    ayv1=mean(vmat1(:,2));
    sdyv1=std(vmat1(:,2));
    azv1=mean(vmat1(:,3));
    sdzv1=std(vmat1(:,3));

    atheta1=mean(thetamat1(:,1));
    sdtheta1=std(thetamat1(:,1));

    athetavar1=mean(varmat1(:,1));
    sdthetavar1=std(varmat1(:,1));

    axrange1=(mean(rangemat1(:,1)));
```

```
sdxrange1=(std(rangemat1(:,1)));
ayrange1=(mean(rangemat1(:,2)));
sdyrange1=(std(rangemat1(:,2)));
azrange1=(mean(rangemat1(:,3)));
sdzrange1=(std(rangemat1(:,3)));

auvar1=mean(uvarmat1(:,1));
sduvar1=std(uvarmat1(:,1));
avvar1=mean(vvarmat1(:,1));
sdvvar1=std(vvarmat1(:,1));
awvar1=mean(wvarmat1(:,1));
sdwvar1=std(wvarmat1(:,1));

aphiwvar1=mean(phiwvarmat1(:,1));
sdphiwvar1=std(phiwvarmat1(:,1));


Drop(1).axv1=axv1
Drop(1).sdxv1=sdxv1
Drop(1).ayv1=ayv1
Drop(1).sdyv1=sdyv1
Drop(1).azv1=azv1
Drop(1).sdzv1=sdzv1

Drop(1).atheta1=atheta1
Drop(1).sdtheta1=sdtheta1

Drop(1).athetavar1=athetavar1
Drop(1).sdthetavar1=sdthetavar1

Drop(1).axrange1=axrange1
Drop(1).sdxrange1=sdxrange1
Drop(1).ayrange1=ayrange1
Drop(1).sdyrange1=sdyrange1
Drop(1).azrange1=azrange1
Drop(1).sdzrange1=sdzrange1

Drop(1).auvar1=auvar1
Drop(1).sduvar1=sduvar1
Drop(1).avvar1=avvar1
Drop(1).sdvvar1=sdvvar1
Drop(1).awvar1=awvar1
Drop(1).sdwvar1=sdwvar1

Drop(1).aphiwvar1=aphiwvar1
Drop(1).sdphiwvar1=sdphiwvar1


axv2=mean(vmat2(:,1));
sdxv2=std(vmat2(:,1));
ayv2=mean(vmat2(:,2));
```

```
sdyv2=std(vmat2(:,2));
azv2=mean(vmat2(:,3));
sdzv2=std(vmat2(:,3));

atheta2=mean(thetamat2(:,1));
sdtheta2=std(thetamat2(:,1));

athetavar2=mean(varmat2(:,1));
sdthetavar2=std(varmat2(:,1));

axrange2=(mean(rangemat2(:,1)));
sdxrange2=(std(rangemat2(:,1)));
ayrange2=(mean(rangemat2(:,2)));
sdyrange2=(std(rangemat2(:,2)));
azrange2=(mean(rangemat2(:,3)));
sdzrange2=(std(rangemat2(:,3)));

auvar2=mean(uvarmat2(:,1));
sduvar2=std(uvarmat2(:,1));
avvar2=mean(vvarmat2(:,1));
sdvvar2=std(vvarmat2(:,1));
awvar2=mean(wvarmat2(:,1));
sdwvar2=std(wvarmat2(:,1));

aphiwvar2=mean(phiwvarmat2(:,1));
sdphiwvar2=std(phiwvarmat2(:,1));

Drop(1).axv2=axv2
Drop(1).sdxv2=sdxv2
Drop(1).ayv2=ayv2
Drop(1).sdyv2=sdyv2
Drop(1).azv2=azv2
Drop(1).sdzv2=sdzv2

Drop(1).atheta2=atheta2
Drop(1).sdtheta2=sdtheta2

Drop(1).athetavar2=athetavar2
Drop(1).sdthetavar2=sdthetavar2

Drop(1).axrange2=axrange2
Drop(1).sdxrange2=sdxrange2
Drop(1).ayrange2=ayrange2
Drop(1).sdyrange2=sdyrange2
Drop(1).azrange2=azrange2
Drop(1).sdzrange2=sdzrange2

Drop(1).auvar2=auvar2
Drop(1).sduvar2=sduvar2
Drop(1).avvar2=avvar2
Drop(1).sdvvar2=sdvvar2
```

```
Drop(1).awvar2=awvar2
Drop(1).sdwvar2=sdwvar2

Drop(1).aphiwvar2=aphiwvar2
Drop(1).sdphiwvar2=sdphiwvar2

maindir=['D:\Drop Structures For Thesis'];
cd(maindir)
save(type{f},'Drop')
```